國立交通大學

光電工程研究所

博 士 論 文

應用於檢測技術的光源設計

The Design of the Light Source for Sensing Technology

研 究 生：周森益

指導教授：祁　甦　教授

中 華 民 國 101 年 六 月

應用於檢測技術的光源設計

The Design of the Light Source for Sensing Technology

研 究 生：周森益　　Student：Sen-Yih Chou

指導教授：祁　甦　　Advisor：Sien Chi

國立交通大學　電機學院

光電工程研究所

博士論文

A Dissertation

Submitted to Department of Photonics and Institute of Electro-Optical Engineering

College of Electrical and Computer Engineering

National Chiao Tung University

in Partial Fulfillment of the Requirements

for the Degree of Doctor of Philosophy

in

Electro-Optical Engineering

June 2012

Hsinchu, Taiwan, Republic of China

中華民國 101 年 6 月

應用於檢測技術的光源設計

學生：周森益　　指導教授：祁甦

國立交通大學光電工程研究所博士班

摘　　要

光學量測技術目前被大量使用在科學研究、工業研發、量產製造及消費性產品上。光學量測技術的主要原理，為使用一光源投射在待測樣品上，待測樣品改變投射光源的光學特性，再由偵測器量出被樣品改變後散射或反射光的光學特性。藉由分析入射與出射光學特性改變，可以量測到待測樣品的特性。因此，檢測技術所使用之光源將影響最後檢測結果之訊噪比。

a. 熱光效應光錐濾波器：本論文組合錐形光纖及光學匹配液構成高斯濾波器，並且藉由熱光效應可以調整濾波器的通過頻帶。借由此濾波器可修正 OCT 的寬頻光源頻譜，並且得到高解析度的生物影像。

b. 超寬頻光源：本論文採用 80fs 的 Ti:sapphire 雷射注入錐形光纖中，產生 400 nm 到 1200 nm 的超寬頻光源。同時採用數值模擬進行超寬頻光源產生過程的動態模擬，探討注入脈衝初始啾頻如何影響超寬頻光源的產生。

c. 單一縱模雷射光源：單一縱模光纖雷射可被應用於光纖通訊、光纖感測器和光譜分析等領域。在此論文中採用雙共振環路限制縱模模態，由摻鉺波導放大器、兩路不等長共振環路及 Fabry-Perot 可調濾波器構成單一縱模光纖雷射。並且討論此雷射架構的輸出強度、側模抑制比、波長及輸出強度的穩定度。

d. 高動態範圍疊紋干涉術：本論文將提出一種利用面型感光元件(CCD 或 CMOS)做單次曝光（one-shot）可得到高動態範圍影像之技術。利用此技術可以得到大範圍且不損失影像細節之高動態影像資料，對此高動態影像進行後續處理，可提高量測之準確度。

The Design of the Light Source for Sensing Technology

Student: Sen-Yih, Chou Advisors: Dr. Sien Chi

Institute of Electro-Optical Engineering

National Chiao-Tung University

ABSTRACT

Optical measurement techniques have been receiving an increasing attention during recent decades. The most important reason is that they work non-intrusively and therefore do not influence the investigated process. The continuing developments in laser, detector, optical fiber and computer technology will further augment the high applicability and versatility of optical measuring techniques. Therefore, it can be expected that optical techniques will continue to gain in importance in many fields of application. However, the procedures of optical measurement techniques include emitted a light signal, this signal modulated by device under test and analyzed the difference of those signal. The purpose of this dissertation is to discuss what is important in optical measurement technology is to adjust the light source suited with this measurement.

誌　　謝

在這個漫長的旅程中，總是有人適時地伸出援手拉我一把，尤其是我的家人永遠在背後默默的支持。衷心地感謝所有幫助過我人，謝謝各位。

目　　錄

圖 目 錄

Chapter 1

Introduction

1.1 Overview of Thermo-Optic Tunable Tapered-Fiber Filter

Fiber-based filters have attracted considerable research interest due to their compact size and low insertion loss for fiber-optic applications. With the existing technologies, band-pass fiber-based optical filters provide different bandwidths ranging. This dissertation presents a novel and simple wideband and band-width-variable bandpass fiber filter using a tapered standard single-mode fiber covered with Cargille liquids. The thermo-optic tunable short-wavelength-pass tapered-fiber filters based on fundamental-mode cutoff mechanism are realized experimentally and analyzed theoretically. The effects of material and waveguide dispersion are investigated and the optimal tapered fiber structures for attaining high-spectral cutoff slope and high-rejection efficiency are determined.

1.2 Overview of the Wideband Tunable Gaussian-Shaped Spectral Filter

Optical liquids can be used to engineer the dispersion characteristics of fibers by serving as the core or cladding to attain fundamental-mode cutoff effect. The short-pass or long-pass fiber filters are so made and concatenated to achieve widely thermo-optic tunable Gaussian-shaped spectral filters. The proposed wideband tunable Gaussian-shaped spectral filter provides a potential technique in application to high resolution bio-imaging.

1.3 Overview of the Supercontinuum Generation in a Tapered Fiber

Relatively wide spectral broadening from above 400 nm to below 1200 nm is generated from a tapered fiber by properly tuning the center wavelength of the pumping 80-fs Ti:sapphire laser. The waist of excited tapered fiber is 1 μm in diameter and only 1-cm long. Additionally, numerical simulation considering the dispersion and nonlinear effect at the transition region of the taper fiber is performed to study the generated supercontinuum spectra. The numerical results show that the nonlinear effect inside the taper transition modifies the pulse shape and phase thus greatly influences the spectral broadening, and using a chirped pulse launching can enhance the efficiency of supercontinuum generation.

1.4 Overview of the Stable and Tunable Fiber Laser

The dissertation proposes and demonstrates experimentally a

single-longitudinal-mode (SLM) fiber double-ring laser using an Erbium-doped waveguide amplifier (EDWA), polarization controller (PC), and a fiber Fabry-Perot tunable filter (FFP-TF) into the ring cavity. In addition, the output power, side-mode suppression ratio (SMSR), and the stabilities of power and wavelength of the laser also are investigated.

1.5 Overview of Projection Moiré Profilometry with High-Dynamic Range Image

As a type of optical measuring apparatus, the charge-coupled diode (CCD) camera provides the capability of increasing the speed of measurement by inspecting an area with only one shot. However, the CCD camera ’ s high-variation range of reflectivity presents an exceptional challenge for the optical measurement established on the surface. The dissertation presents a method that could enable one to acquire an image with a high-dynamic range in one shot without any reduction in spatial resolution. Because of the sufficient signal-to-noise ratio, the method presented could perform the robustness of the phase-retrieving algorithm, and the surface topography could be measured more accurately.

Chapter 2

Analysis of Thermo-Optic Tunable Dispersion-Engineered Tapered-Fiber Filter

2.1 Review of Taper-Fiber Filter

Stronger interaction of the optical evanescent field with the environment has been widely utilized in many fiber-based devices such as the fused-tapered-based fiber filters [1], [2] dispersion-engineering applications [3]–[5] and nanowire sensing applications[6], [7]. The dispersion-engineering techniques manipulate the dispersion characteristics of fiber waveguides to alter the optical properties of fiber devices. In the literatures the theoretical modeling of tapered fibers had been widely developed [8]–[12], the fundamental-mode cutoff effects induced by dispersion-engineering techniques with fiber tapering have not been theoretically investigated yet. The main objective here is thus to theoretically analyze the fundamental-mode cutoff effects and to determine the optimal tapered-fiber structures for achieving low-loss and high-cutoff efficiency. These results should be very crucial for applications such as high-gain low-noise S-band fiber amplifiers [13] and widely tunable S-band fiber lasers [14].

This chapter will present experimental characterization and theoretical simulation results on the studied thermo-optic tunable fused-tapered-fiber filters made

by tapering standard single-mode fibers (SMF-28). The tapered fibers are immersed in Cargille liquids for implementing dispersion engineering through the control of material dispersion. The filter becomes cutoff at longer wavelengths due to the reducing refractive index of Cargille liquids below the effective refractive index of the Cargille liquids below the effective refractive index of the fiber waveguide. The propagation loss increases rapidly near the cutoff wavelength, and a sharp short-wavelength-pass optical filtering edge is achieved. To investigate these effects more deeply, the effective index (n_{eff}) and the mode field diameter (MFD) of the fundamental mode are calculated and carefully examined in order to understand what determines the filter performance. The numerical beam propagation method (BPM) is then adopted to theoretically simulate the cutoff phenomena and the temperature tuning characteristics of the whole device. Good agreement between the simulation and experimental results has been found. Since the filter performance is also significantly influenced by the whole waveguiding structure, the optimal parameters for the uniform taper diameter, uniform taper length, and taper transition length are investigated by the full BPM simulation for achieving best filter performance. From the simulated spectral responses and the effective dispersion curves, find that the taper-waist diameter greatly affects the MFD, which in turn affects the final dispersion relation and the achievable cutoff slope. The taper length can also affect the cutoff slope, and the transition length has direct impacts on the insertion loss. The obtained theoretical results help to determine the optimal device structures for fabricating efficient short-pass tapered-fiber filters which can be utilized in high performance S-band Er-fiber amplifiers and lasers.

2.2 Fabrication Process and Operation Principle

The high-cutoff efficiency of the studied short-pass fiber filter is obtained by locally modifying the material and waveguide dispersion within the uniform taper region. The schematic of the fused-tapered short-pass filter is shown in Fig. 2-1(a). One can describe the structure of a tapered-fiber filter by specifying the transition length (denoted as τ), the uniform waist length (denoted as L_0) and the waist diameter (denoted as ρ). It consists of a transition zone where the diameter is gradually reduced to ρ over a distance τ and then a uniform waist section with the length of L_0. The uniform waist section is immersed within suitable Cargille index-matching liquids. The optical properties of the used Cargille liquids can be summarized as follows. The refractive index $n_D = 1.456$, thermo-optic coefficient $dn_D/dT = -3.74\times10^{-4}/^0C$, and optical transmittance is 88% at 1300nm, and 80% at 1550nm for 1-cm-long length. The whole device is mounted on a thermoelectric (TE) cooler for temperature control. Those tapered-fiber filters are fabricated by a homemade tapering workstation comprising several modules for fiber pulling, heating, and scanning as illustrated in Fig. 2-1(b). A hydrogen flame head with high-accuracy flow control is set on a three axis stepper motor to precisely control the traveling of the flame over the distance of few centimeters. When the tapering process begins, the pulling motors move outward to pull the heated fiber and the flame simultaneously starts to travel back-and-forth for heating the region to be tapered. The pulling mechanism employs a high-precision stepping motor with a right-and-left-threaded screw to drive two V-groove clampers moving outward in a reverse direction. The clampers bilaterally hold the single-mode fiber for providing a precise pulling stress. By controlling the moving speed of the

scanning flame and the pulling clampers, the total elongation length can be varied from 30 to 60 mm, and the corresponding length of the uniform waist is measured to be around 10-25 mm, contingent on the waist diameter. When tapering is finished, the fiber is fixed in a graved U-groove on a quartz substrate and immersed in index-matching liquids. A TE cooler is used to control the liquid temperature to change its refractive index for tuning the cutoff wavelength.

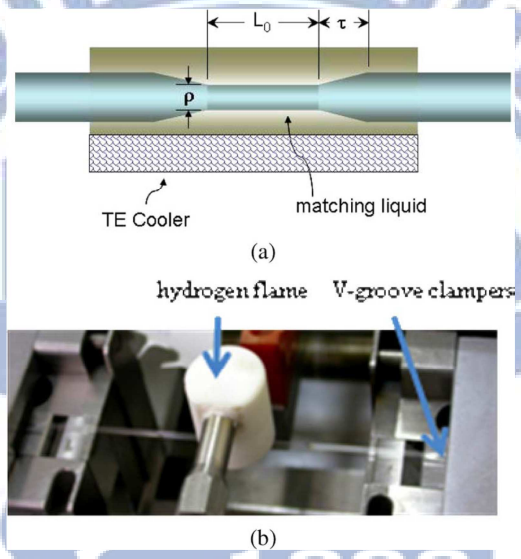

Fig. 2-1. (a) Diagram of a tapered-optical-fiber structure with a uniform waist. (b) Schematic diagram of the tapering station used to fabricate the tapered fibers.

When a single-mode optical fiber is tapered down to few tens micrometer in diameter, the evanescent tail of the mode field spreads out of the fiber cladding and reaches the external environment (Cargille liquids). The size of the Ge-doped core in the tapered zone is so reduced that its waveguiding effects are negligible. Therefore, the pure silica cladding plays as the new core, whereas the external medium serves as the new cladding. The material dispersion curves for the original fiber core (GeO_2 4.1 mol%), cladding (pure silica), and the Cargille liquids are plotted in Fig. 2-2 to illustrate their relative relation. On the righthand side of the cross point indicated in

Fig. 2-2, the refractive index of the liquids is greater than the index of fiber taper and the total internal reflection of the interface is frustrated. Therefore, the lights cannot be guided in the fiber taper and suffer a great amount of optical loss. On the other hand, the light can be nicely confined in the fiber taper when the wavelength is shorter than the cutoff wavelength. The cutoff wavelength of the short-wavelength-pass filter should be very near the cross point of the two dispersion curves indicated in Fig. 2-2, under the condition that the mode in the tapered region is mainly guided by the original cladding. The temperature shift of the cross point as also indicated in Fig. 2-2 provides an intuitive explanation about the temperature-tuning capability of the tapered-fiber filter.

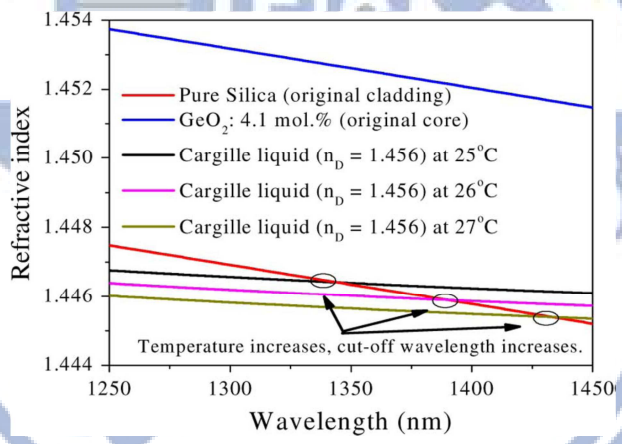

Fig 2-2. Material dispersion curves for the original fiber core (GeO_2 4.1 mol%), cladding (pure silica), and the index-matching liquids measured at 25, 26, and 27°C, respectively.

It should also be noted that a related but different kind of short-wavelength-pass optical filtering effects can be observed when the tapered fiber waist is in the 100 nm range. [15] The tapered fiber is surrounded by the air, and an abrupt change of the mode field diameter as a function of the optical wavelength can be found. This leads to an abrupt change of optical loss accordingly. However, since no dispersion engineering is used to produce true optical cutoff, the filtering slope and rejection

ratio are not as large as the cutoff case studied here.

2.3 Experimental and Simulation Results

Both the experimental and simulated spectral responses of the short-wavelength-pass fiber are displayed in Fig. 2-3 for performance studies and comparison. The solid lines of Fig. 2-3(a)-(c) display the experimental spectral responses of the short-wavelength-pass filter with waist diameters measured to be 20, 26, and 40 μm, respectively. The total elongation lengths are about 30 mm, and the lengths of the uniform waist are measured to be around 18 mm. The larger the waist diameter is, the steeper the cutoff slope can be. Here the cutoff slope (in unit: dB/nm) is defined as the average gradient of the rolloff spectral curve in the linear region from -10 to -30 dB transmission loss. The cutoff slopes are calculated to be -0.54, -1.38, and -2.00 for the cases of ρ = 20μm, ρ = 26μm, and ρ = 40μm, respectively. When ρ = 40μm, the cutoff slope is very sharp, but the rejection efficiency is more limited. The extra loss of less than 2 dB at 1390 nm may result from the absorption of hydroxyl ions which were generated from the hydrogen flame and then diffused into the tapered fiber. The tuning efficiencies of the filter are about 52, 47, and 62 nm/^{o}C for the cases of ρ = 20μm, ρ = 26μm, and ρ = 40μm, respectively. At the guiding wavelengths, the insertion losses of the filters are below 1 dB, 0.5 dB, and 0.3 dB for ρ = 20μm, ρ = 26μm, and ρ = 40μm, respectively. The losses are mainly from the absorption loss of the Cargille liquids and the optical loss due to fiber tapering. The absorption loss caused by the Cargille liquids is estimated to be below 0.2 dB after taking into account the transmittance of the liquids and the evanescent field overlapping effects. The fiber-tapering loss depends on the tapering conditions. In principle, when the

tapering transition is slow enough to meet the adiabatic criteria [16], the tapering loss can be made very small. For our cases, the tapering loss is reasonably low but still observable, as can be seen from the above numbers. Even smaller tapering losses should be possible at the cost of increasing the total device length.

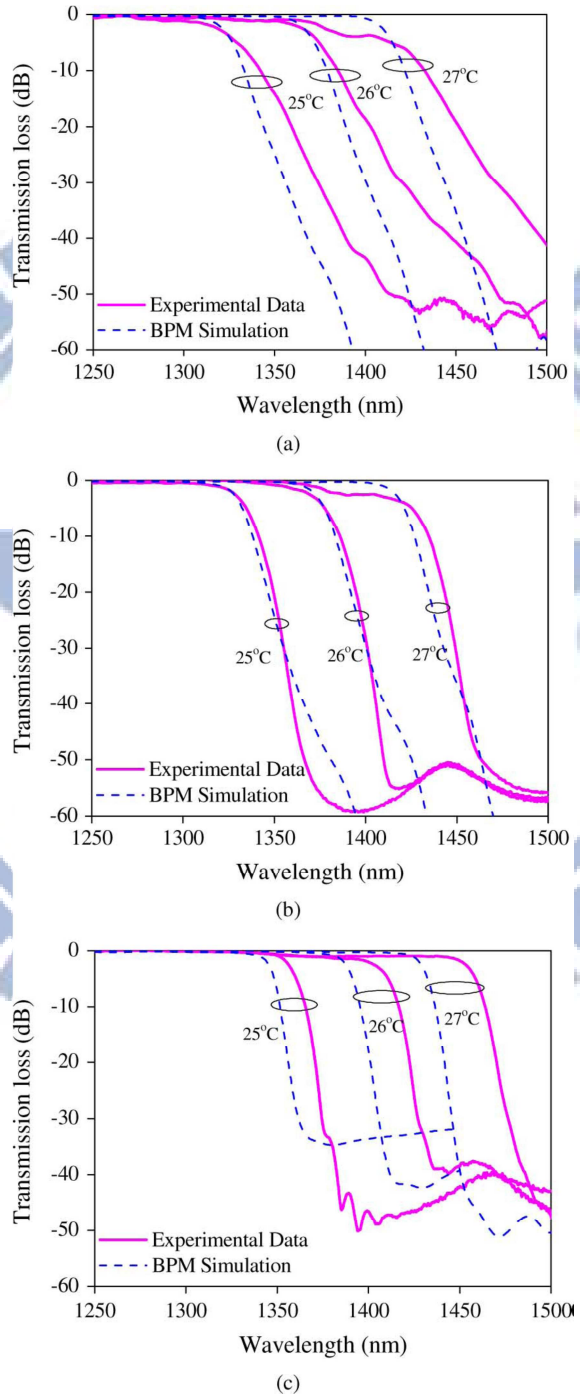

Fig. 2-3. Experimental and simulated spectral responses of the tunable short-wavelength-pass fiber filters for (a) ρ = 20 μm, (b) ρ = 26 μm, and (c) ρ = 40 μm at different temperatures.

To further analyze the fundamental-mode cutoff characteristics, numerical simulation by the BPM is performed to study the optical field propagation within the tapered fibers and to predict the filter performance theoretically. The BPM uses the finite difference method to solve the paraxial approximation of the Helmholtz equation with "transparent" boundary conditions [17]. This approach can automatically include the effects of all the guided and radiation modes as well as the mode-coupling and mode-conversion effects. The fiber-taper transition structure is set to be an exponential shape in our simulation. The dotted lines in Fig. 2-3(a)–(c) show the simulated transmission spectra with the temperatures of 25, 26, and 27 ^{o}C and the waist diameters of 20, 26, and 40 μm, respectively. The cutoff wavelengths gradually shift to longer wavelengths when the temperature increases. Good agreement of the changing trends for the cutoff slopes and rejection efficiencies between the simulated and experimental results has been found. The mismatch of the cutoff wavelengths between the experimental data and simulation results should be due to the uncertainties of the fiber-tapering parameters and the temperature-reading errors in the experiment. Most importantly, the simulation results correctly reproduce the experimental observation that the larger diameter cases have larger cutoff slopes, but will eventually have poorer rejection ratios when ρ is too large (> 40 μm). The thermo-optic-tuning efficiency of the filter for ρ =26 μm in Fig. 2-3(b) is about 48 nm/^{o}C from BPM simulation, which is also in good agreement with the 47 nm/^{o}C tuning efficiency from the experimental data.

Based on the facts that the theoretically predicted tuning and cutoff efficiencies agree reasonably with the experimental data, we further utilize the BPM as a reliable simulation tool to investigate the effects of different taper parameters for determining

the optimal taper structures.

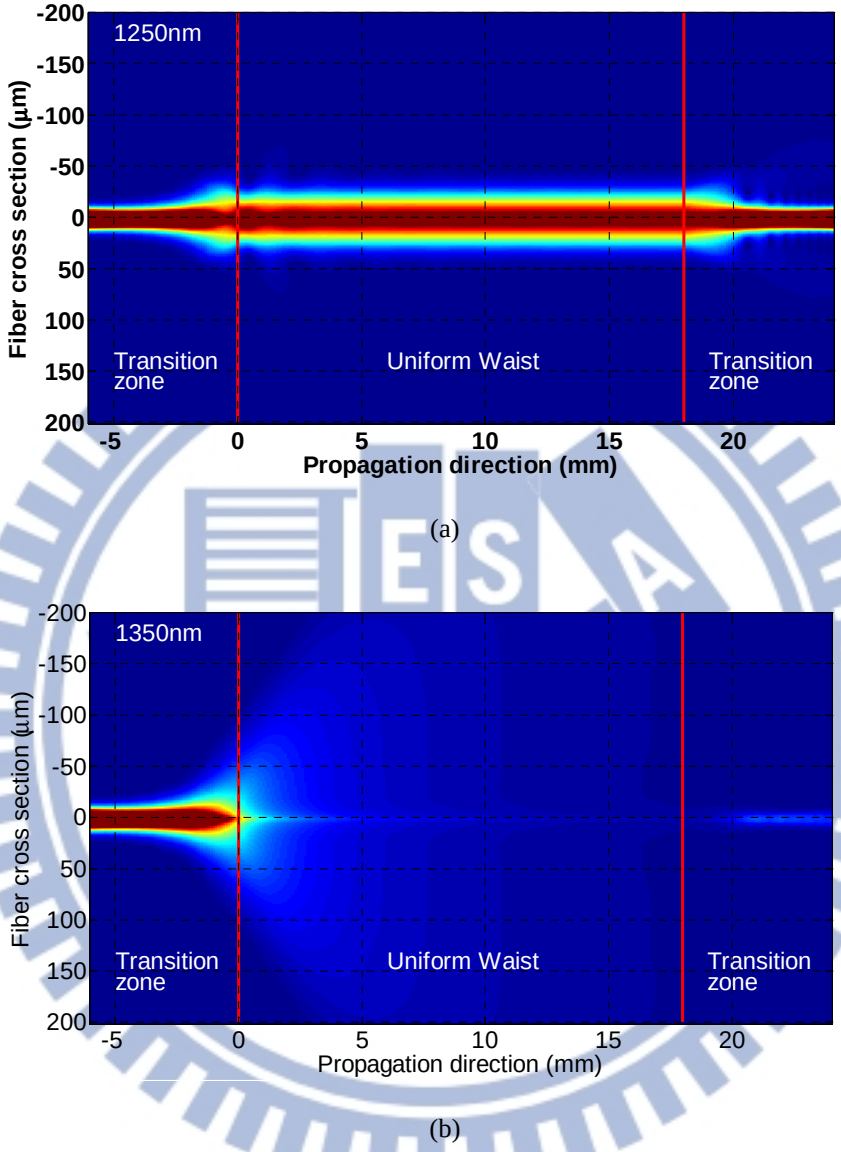

Fig. 2-4. Field distributions along the tapered-fiber filter. (a) When the wavelength (1250 nm) is shorter than the band edge of the filter, the fields are guided over uniform waist and coupled back to the fundamental mode. (b) When the wavelength (1350 nm) is longer than the band edge of the filter, the fields spread out along the uniform waist.

Fig. 2-4(a) and (b) show the simulated field evolution within a tapered fiber with the cutoff wavelength around 1330 nm. The waist diameter ρ is 26 μm, the

transition length τ is 6 mm, the taper transition angle is around 0.5^{o} , the uniform waist length L_0 is 18 mm, and the temperature is set at 25 ^{o}C. In Fig. 2-4(a), when the propagation wavelength (1250 nm) is shorter than the cutoff wavelength, the fundamental eigenmode of the input SMF is smoothly transformed into the fundamental eigenmode of the uniform tapered waist, propagates through the uniform waist region and then gradually reconverts to the fundamental mode of the output SMF within the second transition distance τ . The fundamental MFD is larger in the uniform tapered region when compared to that of the SMF-28. On the other hand, Fig. 2-4(b) shows the case when the propagation wavelength (now 1350 nm) is longer than the cutoff wavelength. The optical field quickly disperses away within the first taper transition region as well as the uniform waist region due to the higher refractive index of the surrounding liquids. Only a very small fraction of the optical field can be coupled back to the fundamental mode of the output SMF. In this way, huge optical losses are induced for wavelengths longer than the cutoff wavelength.

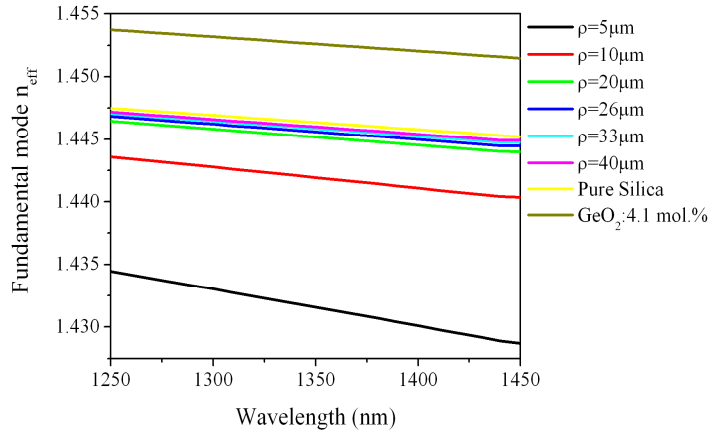

(a)

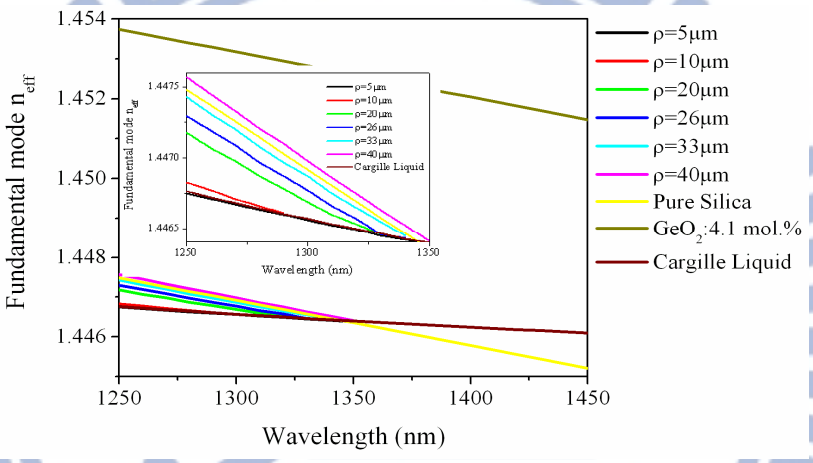

(b)

Fig. 2-5. (a) Effective index of the fundamental mode versus wavelength under different waist diameters of tapered fibers surrounded by (a) the air, and (b) the Cargille liquids (n_D = 1.456).

The material dispersion of the surrounding medium can significantly modifies the dispersion curve of the propagation mode due to the stronger overlap with the evanescent field spread out of the taper waist. To analyze how the surrounding material affects the dispersion properties of the fused-tapered fiber, the effective index of fundamental mode is calculated under different waist diameters of tapered fibers surrounded by the air and the Cargille liquids(n_D = 1.456) . The results are plotted in Fig. 2-5(a) and (b). The material dispersion curves of the original Ge-doped core, the

cladding (pure silica), and the Cargille liquids are also plotted for easy comparison. The index difference of the pure silica and the air is so large that the optical field is strongly confined when the tapered fiber is surrounded by the air. Thus, the dispersion curves of the fundamental mode have almost the same slope ($dn_{eff}/d\lambda = -1.2 \times 10^{-5}$ /nm) with that of the pure silica when ρ >20 μm. The effective mode index is lower than those of the pure silica and Ge-doped core because parts of the optical mode field are now in the air. When the waist diameter gets smaller than 5 μm, the dispersion curve of the fundamental mode becomes more wavelength dependent. This is because now a larger fraction of the mode field is in the air. The slopes of the dispersion curves in Fig. 2-5(b) are calculated to be -0.55×10^{-5}, -0.87×10^{-5}, -0.94×10^{-5}, -1.07×10^{-5}, and -1.14×10^{-5} for ρ =10 μm, ρ =20 μm, ρ =26 μm, ρ =33 μm, and ρ =40 μm, respectively. In contrast, the slopes of the modal dispersion curves for tapered fibers immersed in the Cargille liquids are slightly flatter than those in the air, which indicates that the effective mode index of the tapered fiber is indeed modified by the surrounding dispersive liquids. The insect of Fig. 2-5(b) shows the detailed curves near the cutoff wavelength when the tapered fibers are immersed in the Cargille liquids. The cross points between the dispersion curves of the tapered fibers and the surrounding liquids exactly determine the cutoff wavelength, which will shift to longer wavelengths as the waist diameter increases. When the optical wavelength is near the cross point, the optical field quickly spreads out of the tapered fibers and large optical losses are induced. Intuitively the cross angle between the two intersected dispersion curves determines the cutoff slope. A suitable surrounding material which can produce a larger intersection angle is thus a key for achieving high-cutoff efficiency.

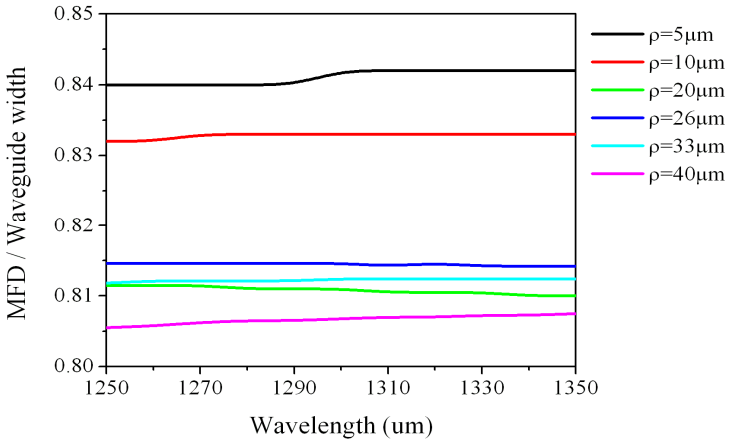

(a)

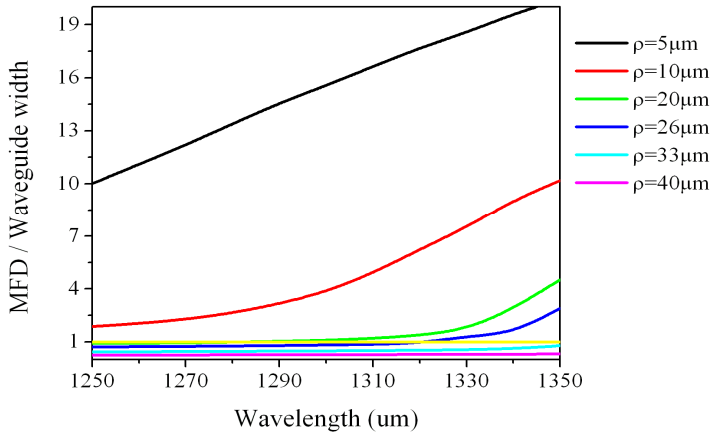

(b)

Fig. 2-6. MFD/waveguide width versus wavelength under different waist diameters of tapered fibers surrounded by (a) the air, and (b) Cargille liquids (n_D = 1.456).

Fig. 2-6(a) and (b) plot the ratio of the 1/e MFD to the waveguide width (waist diameter of the tapered fiber) as a function of the optical wavelength. When the tapered fiber is surrounded by the air, the optical field is strongly confined inside the tapered fiber and thus the width ratio is almost flat with respect to the optical wavelength for the waist diameters considered here. In contrast from Fig. 2-6(b) it is obvious that a larger fraction of the optical field spreads out of the tapered fiber when it is surrounded by the Cargille liquids due to the small index difference. As the waist

diameter is getting smaller, the width ratio gets larger. When the waist diameter is smaller than 10 μm, the optical fields will largely spread out of the tapered waveguide region and will experience higher losses even at guided wavelengths. When the waist diameter is between 20 μm and 26 μm, the width ratio curves exhibit a significant turning point between the guided region and the unguided region, as shown in Fig. 2-6(b). When the waist diameter is larger than 40 μm, the cutoff wavelength is shifted toward the longer wavelengths, and the optical field is more strongly confined in the waveguide. The dispersion-engineered effects can also be seen from the wavelength dependence of the MFD. Fig. 2-7(a) and (b) show the mode field distribution of the fundamental mode in the tapered waist under different taper diameters. Two optical wavelengths at 1250 nm (guiding) and 1350 nm (near cutoff) are used as the examples to illustrate the difference. The field is strongly confined in the tapered region for the guiding wavelengths when $\rho > 20\mu m$. As the waist diameter gets smaller than 10 μm, the field spreads out of the tapered fiber region and larger losses at the guiding wavelengths are produced. Near the cutoff wavelength in Fig. 2-7(b), the field extends more widely into the Cargille liquids due to the weak guiding condition. Thus, the loss becomes huge and the short-wavelength-pass band edge is formed. Moreover, the larger taper diameters ($\rho > 33\mu m$) can confine the fields more tightly than the smaller ones even near the cutoff wavelength.

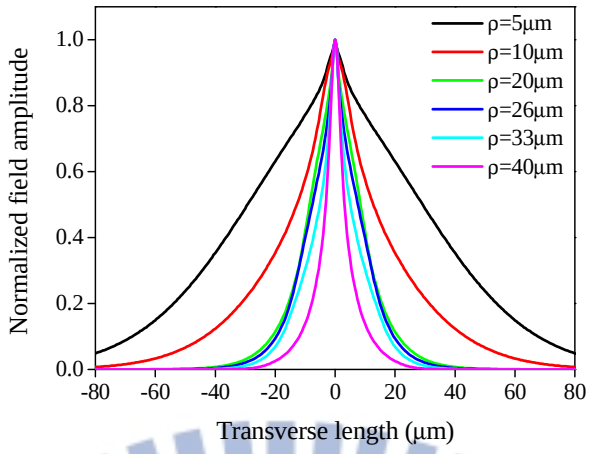

(a)

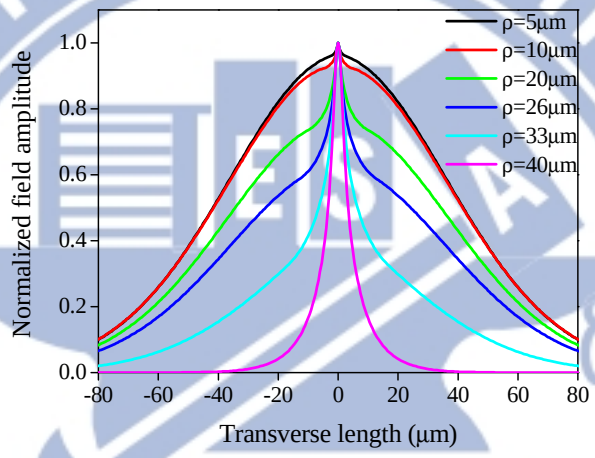

(b)

Fig. 2-7. Fundamental-mode-field distribution in the tapered waist under different taper diameters at (a) 1250 nm (guiding wavelength) and (b) 1350 nm (near cutoff wavelength).

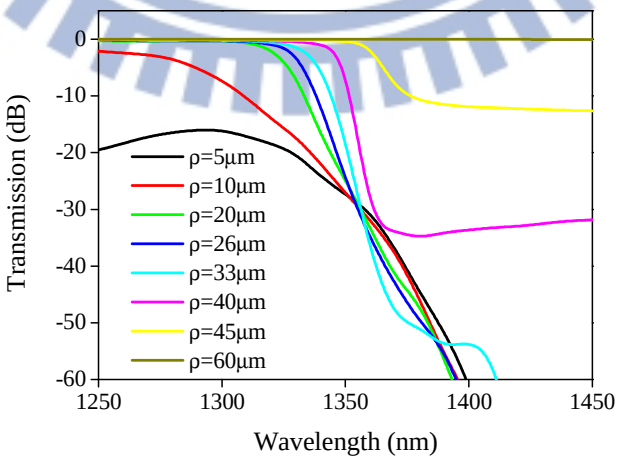

Fig. 2-8. Simulation results of transmission spectra at different waist diameters of 5, 10, 20, 26, 33, and 40 μm, respectively.

Fig. 2-8 shows the simulated transmission spectra of the fiber taper with the waist diameter of 5, 10, 20, 26, 33, 45, and 60 μm, respectively. The fiber transition length τ is 6 mm, the uniform waist length L_0 is 18 mm, and the temperature is at 25°C. The spectral cutoff responses are not the same for different waist diameters. Note that as the waist diameter increases, the band edge is steeper. The cutoff slopes are calculated to be -0.38, -0.79, -1.14, -1.68, and -2.01 for ρ = 10μm, ρ = 20μm, ρ = 26μm, ρ = 33μm, and ρ = 40μm, respectively. The band-edge shifts to the longer wavelengths as the diameter increases. The cutoff characteristics in Fig. 2-8 can be described by the waveguide dispersion behavior with different waist diameters. The optical field intensely spreads out into the Cargille liquids when the waist diameter is getting small. The ratio of the optical field distributed in the waveguide with respect to that in the Cargille liquids is strongly decisive to the effective index of the mode field. When the diameter is less than 10μm, the waist is too thin to confine the optical field. Furthermore, when the waist diameter is getting thinner, most optical field extends into the Cargille liquids, the wave-guiding ability is weaker, and thus the transmission loss becomes larger. The simulation results indicate that the larger the waist diameter is, the steeper the filter cutoff slope can be. However, when the waist diameter is larger than 40μm, the achievable spectral contrast (or rejection efficiency) is more limited due to the stronger mode confinement. The short-wavelength-pass bend edge disappears when the tapered waist is larger than 60μm. All the wavelengths are now strongly confined in the Ge-doped fiber core. Thus, the optimal waist diameter for fused-tapered SMFs to produce a sharp short-wavelength-pass band edge should be somewhere between 33μm and 40μm.

Table 2-I lists the cutoff slopes and dispersion slopes for the waist diameters of 5, 10, 20, 26, 33, and 40μm, respectively. When the waist diameter is larger, the

dispersion slopes are larger and the cutoff slopes are steeper. It also can be clearly seen that steeper cutoff slopes are associated with larger cross angles between the dispersion curves of the tapered fibers and the surrounding liquids. The good agreement of the cutoff slopes from experimental and simulated results confirms that the simulation can help predict the filter performance.

TABLE 2-I

THE CUTOFF SLOPES AND DISPERSION SLOPES FOR DIFFERENT WAIST DIAMETERS OF TAPER FILTERS IMMERSED IN CARGILLE LIQUID

Taper diameter	Dispersion slope Δn_{eff} / nm ($\times 10^{-5}$)	Cutoff slope dB / nm	
10 μm	-0.55	-0.38(simulation)	
20 μm	-0.87	-0.79(simulation),	-0.54(experimental)
26 μm	-0.94	-1.14(simulation),	-1.38(experimental)
33 μm	-1.07	-1.68(simulation)	
40 μm	-1.14	-2.01(simulation),	-2.00(experimental)

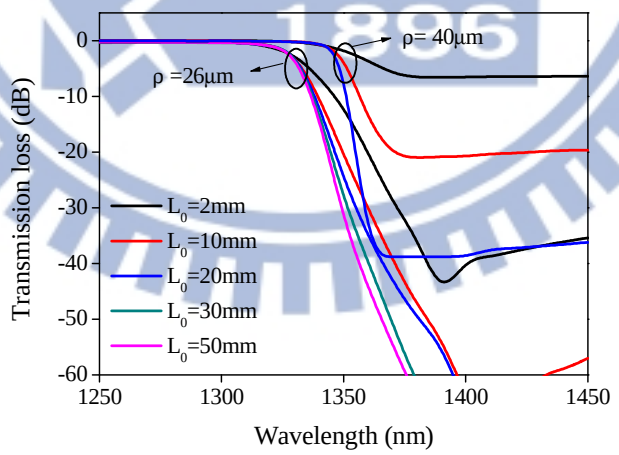

Fig. 2-9. Transmission spectra associated with different lengths of uniform waist of 2 mm, 10 mm, 20 mm, 30 mm, and 50 mm for ρ = 26 μm and 2mm, 10mm, 20mm for ρ =40 μm with the taper transition length of 6 mm.

Fig. 2-9 indicates that the length of the uniform waist also has certain influences

on the cutoff slope of the filter's band edge. The simulation is performed under the assumption that the temperature is 25^{o}C, the fiber taper waist diameter and the waist length are ρ = 26 and 40μm, respectively, and the transition length is τ = 6mm. The tapers have the waist length of 2, 10, 20, 30, and 50 mm for ρ = 26μm and the waist length of 2, 10, 20 mm for ρ = 40μm, respectively. It can be seen that the longer length leads to a steeper band edge for ρ = 26μm. When the waist length is shorter than 30 mm, the cutoff slopes of the band edge significantly increase with the waist length. Since the optical loss is proportional to the taper length, it is not surprised that longer taper length causes higher cutoff loss and thus provides a sharper cutoff slope. However, when the waist length is longer than 30 mm, the cutoff slopes become saturated. For ρ = 40μm, the length of the uniform waist not only influences the cutoff slopes but also affects the rejection efficiencies. The rejection efficiency relies on the sufficient cutoff loss of long taper length. At ρ = 40μm, the optical field is more confined in the tapered waist, and thus the optical cutoff loss is more limited. Since the simulation results indicate that the longer the taper length is, the steeper the filter cutoff slope can be, the optimal waist length for fused-tapered SMF-28 should be at least larger than 20 mm.

To further investigate how the waveguide structure influences the cutoff slopes and optical losses, the taper transition length is varied from 3 mm (taper transition angle around 1.0^{o}), 6 mm (taper transition angle around 0.5^{o}), to 12 mm (taper transition angle around 0.2^{o}). The tapered fiber has a fiber taper waist diameter ρ = 26μm and the waist length L_0 = 18mm. The obtained spectral responses are shown in Fig. 2-10. The smaller filter transmission losses in the shorter wavelength side indicate that longer taper transition length can more guarantee low-loss conversion from the SMF-28 region to the taper region. At guiding wavelengths, the insertion

loss of the filter is below 1.1 dB, 0.3 dB, and 0.01 dB for the cases of τ = 3mm, 6 mm, and 12 mm. The loss difference for guided wavelengths can be as high as 1 dB between τ = 3 and τ = 12mm. The optimal design of the ratio between the taper transition length to the taper diameter should be at least larger than 6 mm/26 μm (i.e., the transition angle of the fiber structure should be less than 0.5^{o}). Based on the above theoretical analyses, the optimal design parameters for the taper waist diameter, waist length, and transition length should be somewhere around 26–40μm, 30 mm, and 6 mm, respectively.

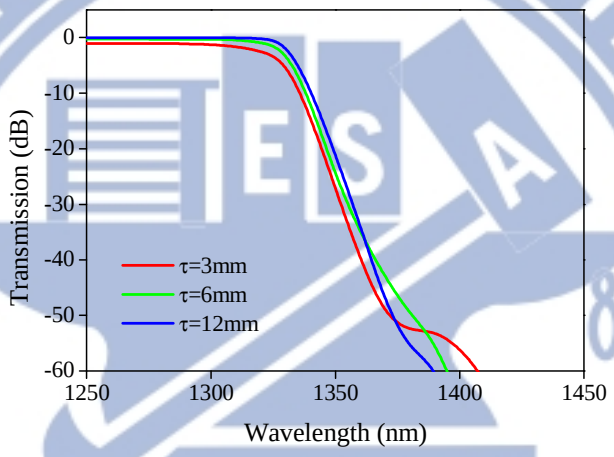

Fig. 2-10. Transmission spectra associated with different transition lengths of 3mm, 6mm, and 12mm with the waist length of 18 mm for ρ =26 μ m.

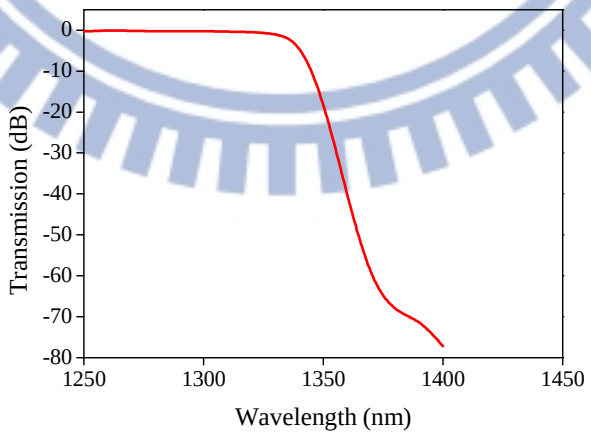

Fig. 11. Transmission spectra of the final optimal design of the short wavelength pass filter. The taper waist diameter is 35 μ m, the waist length is 30 mm, and the transition length is 6 mm.

As the final verification, we set the taper waist diameter, waist length, and transition length to be 35μm, 30mm, and 6mm, respectively, and perform the BPM simulation. The calculated spectral response is shown in Fig. 2-11. The rejection efficiency is as high as 70dB, the cutoff slope is as high as -2.4dB/nm, and the insertion loss is less than 0.3dB. These results indicate the performance improvement that can be expected by carefully adjusting the device parameters.

The aim of this work investigated the influences of the taper length, taper diameter, and transition length on the spectral cutoff slope and rejection ratio of the tapered-fiber filter. The optimization is not absolute in the sense that additional constrains need to be considered. For example, the total length of the device cannot be too long for the ease of practical fabrication. Through this kind of optimization, we can know how much performance improvement can be expected by practically adjusting the device parameters. The Cargille liquids provide a cost-effective, simple, and fast way to implement the fundamental-mode cutoff mechanism.

2.4 Conclusion

In summary, a new type of thermo-optic tunable short-wavelength-pass fiber filters based on fiber tapering and dispersion engineering has been demonstrated experimentally and analyzed theoretically. Good agreements between the BPM simulation and experimental results are achieved. The effects of material dispersion and waveguide dispersion characteristics have been investigated by examining the spectral response as well as the changing trends of the MFD and the effective mode index. An optimized tapered fiber filter structure that can attain high-cutoff efficiency has been suggested based on the obtained theoretical simulation results. It finds for

SMF-28 raw fibers, the uniform tapered waist diameter should be around 35μm, the uniform tapered-waist length should be greater than 30 mm, and the tapered-transition length should be greater than 6 mm. With such an optimized structure, the cutoff slope can be as high as -2.4dB/nm, the rejection efficiency can be as high as 70dB, and the fundamental mode-coupling loss is below 0.3dB. In principle, if different choices of raw fibers can be used, it is possible that the performance can be even more optimized. The analyses presented in the present work should be helpful for developing inline tapered fiber filters based on the dispersion-engineered fundamental-mode cutoff mechanism.

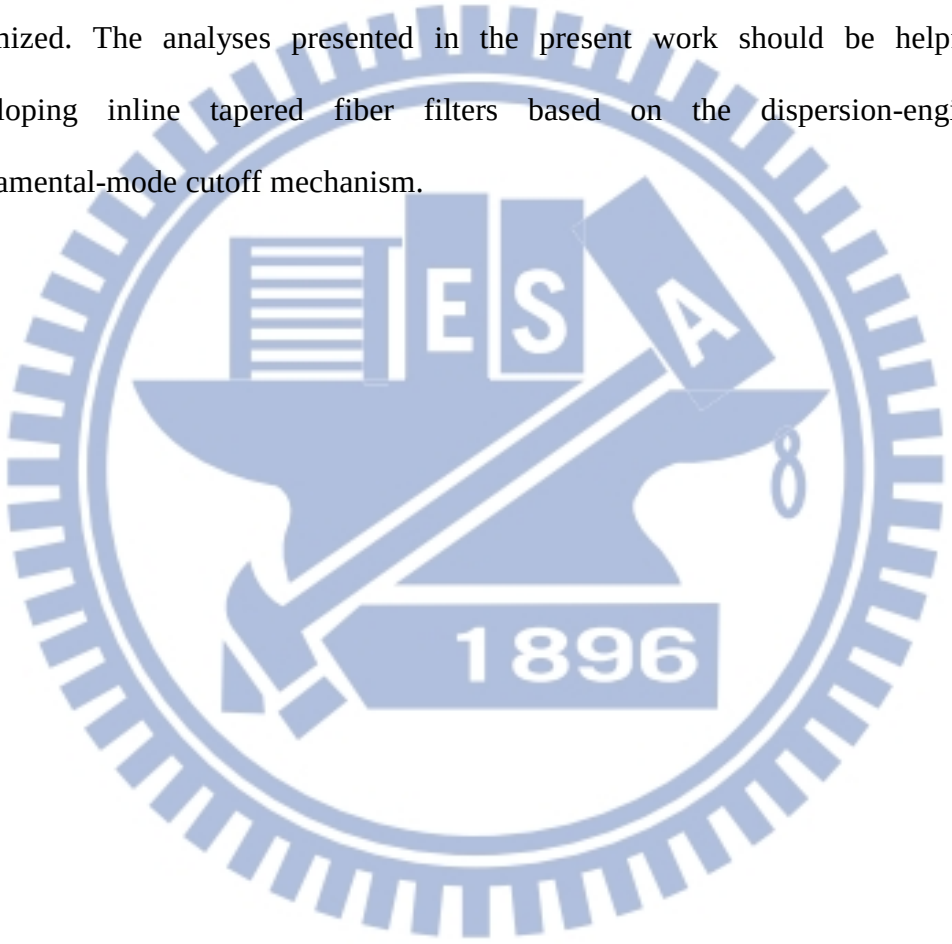

References

[1] W. Ding and S. R. Andrews, “Modal coupling in surface-corrugated long-period-grating fiber tapers,” *Opt. Lett.*, vol. 33, no. 7, pp. 717-719, 2008.

[2] Y. Li and L. Tong, “Mach-Zehnder interferometers assembled with optical microfibers or nanofibers,” *Opt. Lett.*, vol. 33, no. 4, pp. 303-305, 2008.

[3] J. Lou, L. Tong, and Z. Ye, “Dispersion shifts in optical nanowires with thin dielectric coatings,” *Opt. Express*, vol. 14, no. 16, pp. 6993-6998, 2006.

[4] C. M. B. Cordeiro, W. J. Wadsworth, T. A. Birks, and P. St. J. Russell, “Engineering the dispersion of tapered fibers for supercontinuum generation with a 1064 nm pump laser,” *Opt. Lett.*, vol. 30, no. 15, pp. 1980-1982, 2005.

[5] J. Villatoro, D. Monzón-Hernández, and D. Luna-Moreno, “In-line tunable band-edge filter based on a single-mode tapered fiber coated with a dispersive material,” *IEEE Photon. Technol. Lett.*, vol. 17, no. 8, pp. 1665-1667, 2005.

[6] F. Warken, E. Vetsch, D. Meschede, M. Sokolowski, and A. Rauschenbeutel, “Ultra-sensitive surface absorption spectroscopy using sub-wavelength diameter optical fibers,” *Opt. Express*, vol. 15, no.19, pp. 11952-11958, 2007.

[7] G. Brambilla, G. Senthil Murugan, J. S. Wikinson, and D. J. Richardson, “Optical manipulation of microspheres along a subwavelength optical wire,” *Opt. Lett.*, vol. 32, no. 20, pp. 3041-3043, 2007.

[8] T. Birks and Y. Li, “The shape of fiber tapers,” *J. Lightw. Technol.*, vol. 10, no. 4, pp. 432-438, 1992.

[9] S. Xue, A. van Eijkelenborg, G. W. Barton, and P. Hambley, “Theoretical, numerical, and experimental analysis of optical fiber tapering,” *J. Lightw. Technol.*, vol. 25, no. 4, pp. 1169-1176, 2007.

[10] M. Sumetsky, “How thin can a microfiber be and still guide light?,” *Opt. Lett.*,

vol. 31, no. 7, pp. 870-872, 2006.

[11] M. Sumetsky, “Optics of tunneling from adiabatic nanotapers,” *Opt. Lett.*, vol. 31, no. 23, pp. 3420-3422, 2006.

[12] R. Zhang, X. Zhang, D. Meiser, and H. Giessen, “Mode and group velocity dispersion evolution in the tapered region of a single-mode tapered fiber,” *Opt. Express*, vol. 12, no. 24, pp. 5840-5848, 2007.

[13] N. K. Chen, K. C. Hsu, S. Chi, and Y. Lai, “Tunable Er^{3+} -doped fiber amplifiers covering S and C+L bands over 1490-1610 nm based on discrete fundamental-mode cutoff filters,” *Opt. Lett.*, vol. 31, no. 19, pp. 2842-2844, 2006.

[14] N. K. Chen, C. M. Hung, S. Chi, and Y. Lai, “Towards the short-wavelength limit lasing at 1450 nm over $^4I_{13/2} \rightarrow {}^4I_{15/2}$ transition in silica-based erbium-doped fiber,” *Opt. Express*, vol. 15, no. 25, pp. 16448-16456, 2007.

[15] M. Sumetsky, Y. Dulashko, P. Domachuk, and B. J. Eggleton, “Thinnest optical waveguide: Experimental test,” *Opt. Lett.*, vol. 32, no. 7, pp. 754-756, 2007.

[16] J. D. Love, W. M. Henry, W. J. Black, S. Lacroix, and F. Gonthier, “Tapered Single-mode Fibres and Devices Part 1: Adiabaticity criteria,” *IEE Proc. J. Optoelectronics*, vol. 138, no. 5, pp. 343-354, 1991.

[17] R. Scarmozzino and R. M. Osgood, Jr., “Comparison of finite-difference and Fourier-transform solutions of the parabolic wave equation with emphasis on integrated-optics applications,” *J. Opt. Soc. Amer. A*, Vol. 8, no. 5, pp. 724-731, 1991.

Chapter 3

The Wideband Tunable Gaussian-Shaped Spectral Filters

3.1 Introduction

Broadband light sources with high spectral power density are important for high resolution optical coherence tomography (OCT) in cellular or tissue bio-imaging [1]–[3]. The broadband light source with a smooth Gaussian power spectrum is advantageous to achieve low speckle noise, generating from the mutually coherent scattering photons from biological tissues. Echo free OCT imaging can be obtained since a non-Gaussian-spectrum light source will significantly distort the OCT axial point spread function [4] ,[5]. For non-Gaussian-spectrum light sources, the spectral modulation can cause echoes entering the axial point spread function, and the non-exponentially decay tails can cause the blindness of the weak reflection signals [5] to degrade the imaging. A Gaussian filter is usually required to shape the broadband light source into a Gaussian-spectral profile and to stabilize the output wavelengths. Gaussian-spectral filters are also widely used in various areas besides broadband light source imaging applications. For example, these filters are employed in the fiber laser cavity to shape the spectral profile of the laser output lights or in the optical communication systems to stabilize the system operation [6] – [8]. So far, the

proposed Gaussian filters were made of a linear temperature gradient chirped fiber Bragg grating [9] or a large mode area photonic crystal fiber (PCF) filled with high index liquid crystal (LC) in the holey cladding [10]. However, the typical passband bandwidth of the fiber Bragg grating may be too narrow to be used for the practical OCT systems and for the PCF fibers, the tuning efficiency is not very high due to the low temperature gradient of LC. The use of LC would also introduce extra birefringence for the guiding lights. Moreover, the Gaussian-shaped spectrum can only be obtained at certain fixed temperatures of LC and the bandwidth is not tunable.

In this chapter, it proposes a new type of widely tunable Gaussian shaped spectral filters by concatenating a short-wavelength-pass filter (SWPF) and a long-wavelength-pass filter (LWPF). The falling (rising) spectral curve of the SWPF (LWPF) is dispersion-engineered to fit the right (left) wing of the Gaussian profile through carefully adjusting the material and waveguide dispersions. For short-wavelength-pass filter, the refractive index dispersion (RID) discrepancy between the optical liquid and silica tapered fiber is so large that the total internal reflection (TIR) criteria can only be satisfied at the wavelengths shorter than the cutoff point and the widely tunable short-pass filters are achieved accordingly. The tuning range is at least wider than 400 nm (1250–1650 nm) with a tuning efficiency higher than 50nm/^{o}C and the filtering efficiency (slope of falling curve) can be maintained when the cutoff wavelength is tuning far away from the origin [11], [12]. Based on the same principle, a local liquid-core single-mode fiber was used to achieve widely tunable long-pass filters [13] and finally a bandpass filter with a wide tuning bandwidth can be made by concatenating one short-pass and one long-pass filters. The spectral envelope of the bandpass filter can be further engineered to fit the Gaussian profile based on the modification of the waveguide dispersion determined

by the fiber diameter and the modification of the interaction length. Consequently, based on the material and waveguide dispersion engineering achieves a widely tunable broadband all-fiber Gaussian-shaped spectral filter by concatenating a short-wavelength-pass filter and a long-wavelength-pass filter. Preliminary experimental and theoretical results show that the generated Gaussian-spectral lights can have a spectral contrast ratio higher than 40 dB, which should be useful for the OCT bio-imaging applications.

3.2 Simulation and Experiment

To achieve spectral Gaussian filters operating over 1250 – 1650nm, a long-wavelength-pass filter with a rising Gaussian-shaped cut-on curve at the shorter wavelength side and a short-wavelength-pass filter with a falling Gaussian shaped cutoff curve at the longer wavelength side are discretely employed. The refractive index dispersion curves for the various Cargille liquids (Cargille index-matching liquid with the index n_D = 1.456 and the thermo-optic coefficient $dn_D/dT = -3.74 \times 10^{-4}/℃$) and the fused silica glass are shown in Fig. 3-1(a). The liquids have a flatter refractive index dispersion slope than fused silica due to their lower phonon energies [13]. In Fig. 3-1(a), the cross point of the refractive index dispersion curves of the silica and optical liquid (n_D = 1.456) are labeled by P. From the two refractive index dispersion curves, in the left-hand side of P point short-wavelength-pass filters can be achieved when the fused silica and optical liquid respectively plays as the core and cladding [12]. Light guiding is only satisfied for the wavelengths shorter than the P point but frustrated at other side of P point and thus great amounts of optical losses are introduce there. On the contrary, in the right-hand

side of P point long-wavelength-pass filters can be realized when the roles played by the fused silica and optical liquid are reversed [13]. The cross angle θ between the two refractive index dispersion curves decides the filtering efficiency and a larger θ can more clearly discriminate the passband and stopband wavelengths and gives rise to a sharper rising or falling curve for the filters. A very sharp rising or falling curve is crucial for the fiber-optic communication systems to clearly separate the desired and unwanted signals but may not be suitable for the low coherence tomography imaging systems in which a broadband Gaussian light source is required to obtain high quality images. A broadband Gaussian spectrum naturally comes along with slowly varying rising and falling spectral curves and therefore the spectral envelope of the bandpass filter must be further adjusted. The adjustments of the slope for rising and falling curves of filters can not only be done by engineering the material dispersion, namely the use of suitable liquids, but also by engineering the waveguide dispersion, namely the modification of the fiber structure. It can reshape the rising and falling curves to fit the Gaussian profile by selecting suitable diameter of tapered waist D, length of tapered waist L_W, and length of tapered transition L_T. The cutoff and cut-on curves of the short-wavelength-pass filters and long-wavelength-pass filters are numerically simulated by adopting the beam propagation method (BPM) to determine the optimal waveguide structures for an ideal Gaussian-shaped spectrum and some experimental results are demonstrated to show the thermo-optic tuning ability. Further optimized can be taken in the future to attain better Gaussian-shaped spectral filtering function.

Numerical simulation using the beam propagation method (BPM) is performed to theoretically analyze the fundamental mode cutoff characteristics and study the optical field propagation within the tapered region of the standard single-mode fibers. The fiber taper transition structure is set to be an exponential shape, and a

fundamental fiber mode is launched into the transition region to estimate the mode coupling and mode conversion effects along the fiber taper with dispersive liquids surrounded. The fundamental eigenmode of the input SMF fiber is smoothly transformed into the fundamental eigenmode of the uniform taper waist, and the field propagates through the uniform waist region and then gradually re-converts to the fundamental mode of the output SMF within the second transition zone. The fundamental modes corresponding to wavelengths with 10-nm separation are sequentially launched into the tapered fiber, and the output optical powers normalized to the input powers are estimated as transmission loss. BPM simulations with different taper parameters for short-wavelength-pass filters and long-wavelength-pass filters are respectively performed for determining the optimal taper structures to yield the half part of the spectral Gaussian shape. The simulated transmission spectra of the short-wavelength-pass filter and long-wavelength-pass filter are respectively shown in Fig. 3-1(b) and (c) with the key parameters indicated. In Fig. 3-1(b), when D gradually goes down toward 10μm, the slopes of the falling curves get flatter since the waveguide dispersion only dominates the net dispersion at smaller D. Thus a smaller D can make the shorter wavelengths more lossy. The curve of D = 10μm can fit the Gaussian profile quite well and the attenuation can be as high as 80dB. When this Gaussian fit falling curve combined with its mirror image to form a complete Gaussian profile, a broadband Gaussian signal with strong spectral contrast can be generated.

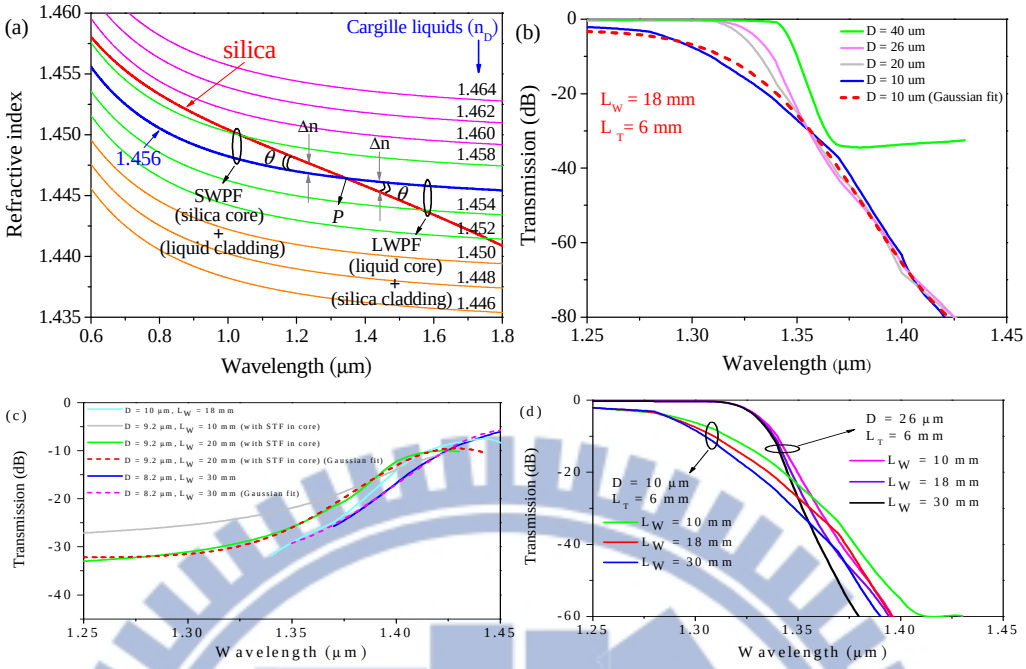

Fig. 3-1. (a) Refractive index dispersion of silica and Cargille optical liquids. (b) Simulated transmission spectra of the SWPFs at different diameters of tapered waist and the Gaussian fit curve. (c) Simulated transmission spectra of the LWPFs at different diameters of liquid core and the Gaussian fit curves. (d) Simulated transmission spectra of the SWPFs at different lengths of tapered waist.

For the long-wavelength-pass filters, the fabrication method is by stretching a borosilicate capillary with a threaded submicron tapered fiber inside, until the inner diameter of the capillary decreases to a few micrometers. The stretched capillary with a submicron tapered fiber inside is then infiltrated with optical liquids to act as a new core, and long-wavelength-pass filters can thus be achieved. The mode fields of the guiding lights are strongly extended to the outside of submicron tapered filter and tightly overlapped with optical liquids. The dispersion of the guiding lights can be strongly changed by the local liquid-core/borosilicate-cladding structure [13]. In Fig. 3-1(c), a submicron tapered fiber with a liquid-core diameter D of 950 nm [13] is also simulated to engineer the dispersion for the best Gaussian fit. The slope of the rising curve and the attenuation for long-wavelength-pass filters are flatter and smaller than

that of short-wavelength-pass filters. This is because even when the long-wavelength-pass filter and short-wavelength-pass filter are using the same silica and optical liquid to produce the same θ and the same index difference Δn near P point in Fig. 3-1(a), the mode field distribution is larger at the longer wavelength side for the long-wavelength-pass filters and thus the poor confinement leads to a flatter cut-on curve and smaller spectral contrast. However, a longer L_W can be utilized to achieve a shaper cut-on curve for Gaussian fitting and, from Fig. 3-1(c), the rising curves of the long-wavelength-pass filters can also fit the desired Gaussian profiles. Simulated transmission spectra of the short-wavelength-pass filters at different length of tapered waist are also shown in Fig. 3-1(d). The adjustment of L_W can also help to fit the Gaussian profile for the cases of smaller D.

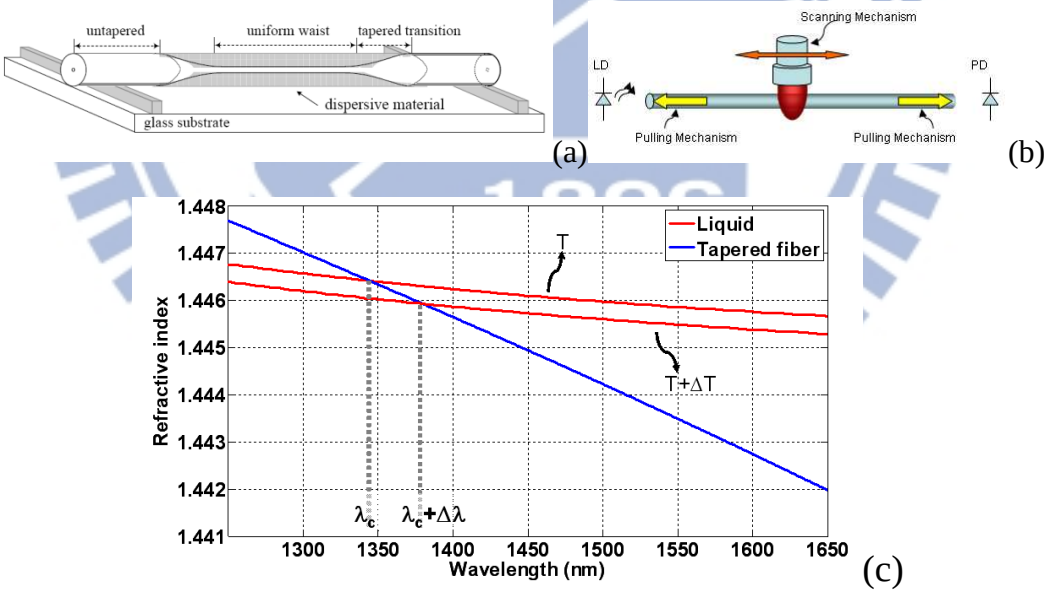

Fig. 3-2. (a) Diagram of a tapered optical fiber (SWPF) with a uniform waist. (b) Schematic diagram of the tapering station used to fabricate the tapered fibers. (c) Refractive index dispersion curves with different temperature. The solid line depicts the tapered fiber, and the dotted line indicates the index matching liquid with different temperatures. (d) Spectral responses and fitted Gaussian curves of SWPF at different temperatures.

The spectral Gaussian filter can be achieved by combining a rising-Gaussian cut-on curve from the short-wavelength-pass filter and a falling-Gaussian cutoff curve from the long-wavelength-pass filter. To generate the falling-Gaussian cutoff curve, Fig. 3-2(a) shows the waveguide structure of the short-wavelength-pass filter. It consists of a transmission zone, where the fiber diameter gradually reduced over the distance, and a uniform-waist section in the middle. The fused–tapered fiber is immersed with index-matching liquids, and the optimal D is around 10μm by simulation, seen from Fig. 3-1(b). The total elongation length is about 30 mm, and the length of the uniform waist is measured to be around 18 mm. The tapered fiber filter fabricated by our homemade tapering workstation which integrates several parts including the pulling mechanism, heating system, scanning mechanism, and real-time monitor system, as has been shown in Fig. 3-2(b). A hydrogen flame with stabilized flow control set on a three-axis stepper motor forms the main part of the heating system and scanning mechanism. This setup allows precise positioning of the flame and the flame is allowed to scan over a large heating-zone. When the tapering process begins, the pulling motors move outward to elongate the fiber and the flame starts simultaneous zigzag scanning to enlarge the effective heating-zone. This process ensures that the flame heats identically each section of the fiber being tapered in each cycle of scanning. As long as the heating-zone can be controlled precisely, the length of the uniform waist of the tapered fiber is controllable. The pulling mechanism has two high-precision stepper motors with simultaneous start/stop design and drives two V-groove holders that can mount a single-mode fiber and provide a constant stress. One end of the single-mode fiber is connected to superluminescent diodes (SLD) and the other end is connected to a photo-detector (PD) to form a real-time monitoring

system, which can help determine the best stop-point for the stretching procedure. When finishing tapering, the fiber is fixed in a U-groove on a quartz substrate and then immersed in index-matching liquid. A TE-cooler is used to control the liquid temperature to change its refraction index and the cutoff wavelength turns out to be tunable. When a single-mode optical fiber is tapered to tens of micrometers in diameter, the evanescent waves spread out into the cladding and reach the external environment and the size of the core in the tapered zone is so reduced that its waveguiding effects are negligible. Therefore, the cladding plays the role of core and the external medium plays the role of cladding. Fig. 3-2(c) shows the refractive index dispersion curves of the index-matching liquid (red) and tapered fiber (blue) at different temperatures. At the right side of the cross point (λc), the refraction index of the liquid is greater than the index of fiber taper and the total internal reflection is frustrated. Therefore the lights cannot be guided in the fiber taper and suffer great amount of optical losses. On the other hand, the light can be confined in fiber taper when the wavelength is located at the left-hand side of the cross point. The cutoff wavelength of a short-wavelength-pass filter approximately locates at the cross point. As the temperature increases, the refractive index of the surrounding liquid decreases. Heating up the liquid causes the dispersion curve shift downward and the cross point will move to longer wavelengths. By heating up or cooling down the liquid (temperature changes from T to T + $\triangle$T), we can continuously tune the band-edge wavelength, as shown in Fig. 3-2(c). The gray line in Fig. 3-2(d) is the initial cutoff curve of the tapered fiber immersed in optical liquid at room temperature (RT) and the liquid is then heated up by a 175W infrared lamp which is located 20 cm away from the tapered fiber. When the liquid is respectively heated up by the infrared lamp with an increment of 5 s for each run time, three different falling curves are obtained as

shown in Fig. 3-2(d), with their slopes getting flatter and flatter. The P point of the short-wavelength-pass filter moves to longer wavelengths with increasing temperature so that the passband bandwidth becomes wider. The achieved spectral contrast is higher than 40 dB for all curves, which is advantageous for practical applications. The cutoff curves become slowly falling down since the waveguide dispersion significantly dominates the dispersion when D decreases to be less than 10μm. The optical field strongly spread out into the optical liquid and becomes less dispersive. The falling curves are individually Gaussian-fitted and the Gaussian fit curves are also displayed as dotted lines shown in Fig. 3-2(d), where in particular the experimental data of the pink line can fit the Gaussian profile and the simulation results excellently well. In principle, the long-pass filter based on liquid-core fiber [13] can also produce Gaussian-shaped curves as predicted in Fig. 3-1(c). Consequently, the concatenated Gaussian-shaped bandpass filter will be widely tunable ascribing to the high thermo-optic coefficient of optical liquids [13]. The wideband tunable Gaussian-shaped spectral filter can be further optimized by carefully considering both material dispersion and waveguide dispersion. The proposed spectral filter provides a potential technique in application to high resolution bio-imaging.

3.3 Conclusions and Summary

This chapter has proposed a new method of achieving widely tunable all-fiber broadband Gaussian-shaped spectral filters by concatenating thermo-optic tunable short-pass and long-pass filters. The material and waveguide dispersions are both employed to vary the spectral envelope of short-wavelength-pass filters and long-wavelength-pass filters to respectively fit the right and left wings of the desired

Gaussian profile. The achieved spectral contrast can be higher than 40 dB and the filter still keeps Gaussian-shaped during thermo-tuning process. This kind of widely tunable Gaussian filters should be advantageous for optical coherence tomography (OCT) bio-imaging systems using broadband light sources.

References

[1] A. Unterhuber, B. Povazay, K. Bizheva, B. Hermann, H. Sattmann, A. Stingl, T. Le, M. Seefeld, R. Menzel, M. Preusser, H. Budka, Ch. Schubert, H. Reitsamer, P.K. Ahnelt, J.E. Morgan, A. Cowey, W. Drexler, "Advances in broad bandwidth light sources for ultrahigh resolution optical coherence tomography," *Phys. Med. Biol.*, vol. 49, 1235, (2004).

[2] S.K. Dubey, D.S. Mehta, A. Anand, C. Shakher, "Simultaneous topography and tomography of latent fingerprints using full-field swept-source optical coherence tomography," *J. Opt. A: Pure Appl. Opt.*, vol. 10, 015307, (2008).

[3] K. Grieve, G. Moneron, A. Dubois, J. Gargasson, C. Boccara, "Ultrahigh resolution ex vivo ocular imaging using ultrashort acquisition time en face optical coherence tomography," *J. Opt. A: Pure Appl. Opt.*, vol. 7, 368, (2005).

[4] H.S. Djie, C.E. Dimas, D.N. Wang, B.S. Ooi, J.C.M. Hwang, G.T. Dang, W.H. Chang, "InGaAs/GaAs quantum-dot superluminescent diode for optical sensor and imaging," *IEEE Sens. J.*, vol. 7, 251,(2007).

[5] B.E. Bouma, G.J. Tearney, Handbook of Optical Coherence Tomography, Marcel Dekker, New York, 2002 (Chapters 2, 3, and 7).

[6] G. Contestabile, R. Proietti, N. Calabretta, M. Presi, A. D'Errico, E. Ciaramella, "Simultaneous demodulation and clock-recovery of 40-Gb/s NRZ-DPSK signals using a multiwavelength Gaussian filter," *IEEE Photon. Technol. Lett.*, vol. 20, 791, (2008).

[7] A. Chong, W.H. Renninger, F.W. Wise, "Environmentally stable all-normal dispersion femtosecond fiber laser", *Opt. Lett.*, vol. 33, 1071, (2008).

[8] A. D'Errico, "WDM-DPSK detection by means of frequency-periodic Gaussian filtering," *Electron. Lett.*, vol. 42, 112, (2006).

[9] I.C.M. Littler, M. Rochette, B.J. Eggleton, “Adjustable bandwidth dispersionless bandpass FBG optical filter,” *Opt. Express*, vol. 13, 3397, (2005).

[10] L. Scolari, T.T. Alkeskjold, A. Bjarklev, “Gaussian filtering with tapered liquid crystal photonic bandgap fibers,” *in: Proc. of LEOS 2006*, ThN3, 2006.

[11] Kuei-Chu Hsu, Nan-Kuang Chen, Sen-Yih Chou, Shien-Kuei Liaw, Yinchieh Lai, and Sien Chi, “Wideband tunable Gaussian-shaped spectral filters based on dispersion engineering,” *Opt. Fiber Technol.*, vol. 15, 373, 2009.

[12] N.K. Chen, K.C. Hsu, S. Chi, Y. Lai, “Tunable Er3+-doped fiber amplifiers covering S and C+L bands over 1490–1610 nm based on discrete fundamental-mode cutoff filters,” *Opt. Lett.*, vol. 31, 2842, (2006).

[13] N.K. Chen, S. Chi, “Novel local liquid-core single-mode fiber for dispersion engineering using submicron tapered fiber,” *in: Proc. of OFC 2007*, JThA5, 2007.

Chapter 4

The Supercontinuum Generation in a Tapered Fiber

4.1 Introduction

Generation of broadband supercontinuum (SC) has many practical applications [1], and supercontinuum in the literatures is mainly generated in microstructure fibers [2]-[4] as well as photonic nanowires [5]-[7]. Microstructure fibers are good candidates to generate supercontinuum due to the unique waveguide structure that can manipulate the dispersion characteristics and efficiently generate the nonlinear effects, but they often require high cost and special design. For supercontinuum generation in photonic nanowires, a sufficient length and high-index contrast of submicrometer-diameter wires is needed to obtain long interaction length to generate wideband spectra. However, the fabrication of long submicrometer wires was tough by use of simple tapering techniques, and these long tapered fibers are brittle for high-power handling. Recently, the supercontinuum generation and nonlinear phenomenon from planer waveguide is promising for all-optical circuits, and the waveguide design for managing the dispersion becomes important topic because it greatly affects the nonlinear response [8]-[10]. To understand how the waveguide design influences the nonlinear effect can simply start from conventional tapered fiber,

and the discussion of the spectral broadening mainly considering the group velocity dispersion inside the taper waist [11]-[18]. The theoretical study on the influence of taper transition region is often neglected because its relative lower efficiency of nonlinear process compared to the waist region. In recent year, some researchers have noted that must simulate the whole region of a tapered fiber for fairly represent the comprehensive propagation characteristics.

In this chapter, by properly tuning the center wavelength of femtosecond Ti:sapphire laser launched into the home-made tapered fiber, relatively wide spectra from above 400 nm to below 1200 nm can be experimentally observed. The tapered fiber is 1 μm in diameter and only 1-cm in length. Creating a model discusses the femtosecond pulse propagation through the whole region of a tapered fiber theoretically and using split-step FFT method to numerically study the characteristics of supercontinuum generation in tapered fiber. Furthermore, it discusses the transition region of a tapered fiber with different shape that will induce phase chirped and exert a strong influence on the supercontinuum generation.

4.2 Experiment Setup and Results

In this experiment, a simple fiber tapering technique is used to produce low-loss 1-μm-diameter wires from a standard single-mode fiber (SMF-28). The fiber pulling setup consists of a hydrogen torch and two computer controlled linear stages [19]-[20]. A hydrogen flame with stabilized flow control set on a three-axis stepper motor forms the main part of the heating system and scanning mechanism. This setup allows precise positioning of the flame, and the flame is allowed to scan over a large heating-zone. When the tapering process begins, the pulling motors move outward to

elongate the fiber and the flame starts scanning back and forth to enlarge the effective heating-zone. This process ensures that the flame uniformly heats each section of the fiber being tapered in each cycle of scanning. The parameters for the fiber pulling system, such as speed, acceleration, fiber tension and position of the flame, were optimized to yield a uniform waist of about 1-μm in diameter and 1-cm in length. The diameter of the waist is measured around 1 μm, the length of the waist is around 10 mm, and the transition zone has an exponential shape with the length of 45 mm, as shown in Fig. 4-1.

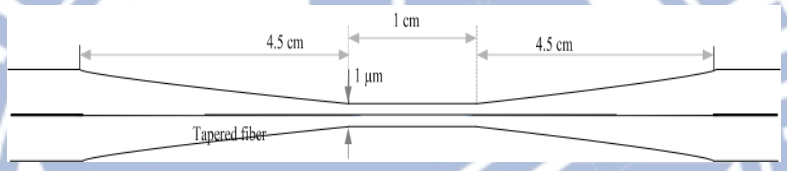

Fig. 4-1. Schematic diagram of the taper fiber structure.

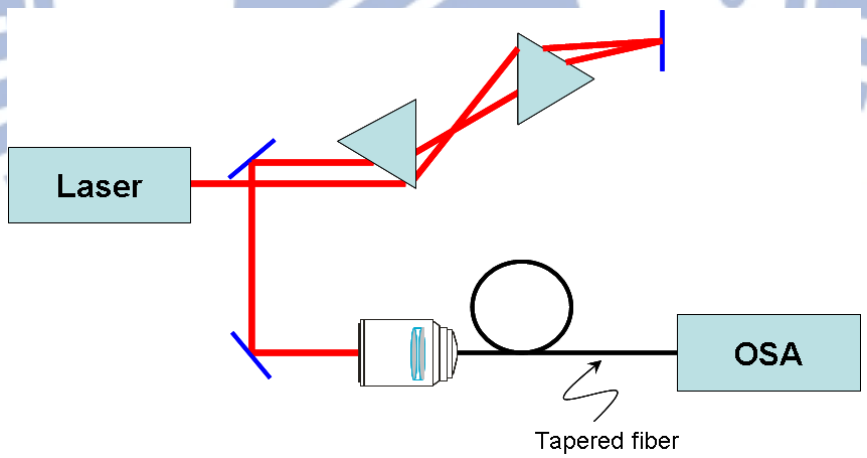

Fig. 4-2. Experimental setup of the supercontinuum generation.

To generate the supercontinuum spectra, the excitation pulses are coming from a tunable femtosecond Ti:sapphire laser (Tsunami, spectral physics inc.), whose center wavelength can be tuned from 700 nm to 900 nm, as shown in Fig. 4-2. Launching 82 MHz and 80 fs pulses into the tapered fiber, the coupling efficiency of the entire

tapered fiber is about 40%. The tapered fiber remains about 45-mm-long standard single-mode on each side that causes substantial dispersion when the pulse propagating through. In order to compensate the normal dispersion from the standard optical fiber, a prism pairs with separation about 20 cm is used to provide the anomalous dispersion. Then an optical spectral analyzer (Ando, AQ 6315) is used to measure the generated spectra.

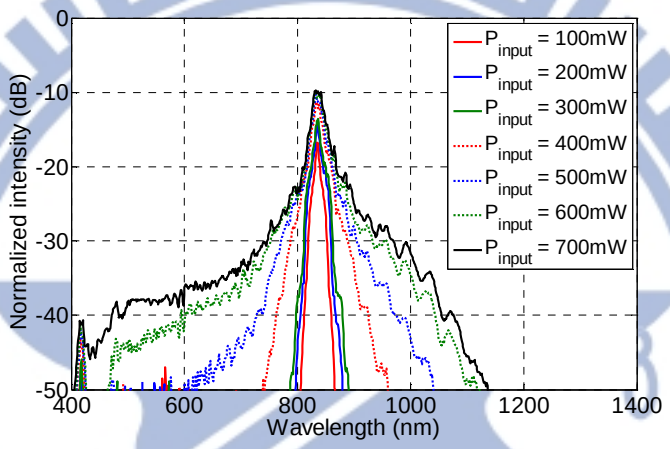

Fig. 4-3. Generated spectra at different pump powers using 1-μm-diameter fiber tapers. The output pattern from the fiber and the dispersed spectra by the prism are shown inset.

Supercontinuum can be generated by properly tuning the center wavelength of Ti:sapphire laser. Using the 1-μm-diameter tapered fiber and choosing the center wavelengths of 830 nm, the generated spectra at different exciting powers are shown in Fig. 4-3. Notice that the second harmonic wave (around 415 nm) can be generated due to destroy of the centosymmetric. At lower pump power (100 mW to 250 mW), the spectrum is broaden initially due to the self-phase modulation (SPM). As pumping power increases (400 mW to 500 mW), the extension of generated spectra in the longer wavelength are obvious than in the shorter wavelength due to stimulated

Raman scattering. Increasing the pump power (>500 mW) will slow down the extension of generated spectra in the longer wavelength edge. Nevertheless, the generated power in short wavelength becomes strong due to the four waves mixing. The output pattern and the spanning spectra after the prism are also shown the inset of Fig. 4-3. The spectral bandwidth $\Delta\lambda$ defined at the detuning wavelength with intensity of -20 dB to that at peak wavelength is around 190 nm at 400 mW input power, and 430 nm at 700 mW input power.

4.3 Simulation and Discussion

Numerical simulations are carried out to explain the experimental observations. There are numerous numerical simulation studies on supercontinuum generation in tapered fibers, and typically supercontinuum generation in a biconical tapered fiber is theoretically investigated using nonlinear Schrödinger equation as numerical model [13]-[19]. The nonlinear Schrödinger equation can be expressed as

$$\frac{\partial A}{\partial z}+\frac{\alpha}{2}A-\sum\frac{i^{n+1}}{n!}\beta_n\frac{\partial^n A}{\partial t^n} = i\gamma\left(1+\frac{i}{\omega_0}\frac{\partial}{\partial t}\right)\left(A(z,t)\int_{-\infty}^{\infty}R(t')\,|A(z,t-t')|^2\,dt'\right) \tag{4.1}$$

where A is the amplitude of the pulse envelope, α is the absorption coefficient, t is the time, and z is the propagation axis along the fiber. The β_n are nth-order dispersion coefficients, and ω_0 is the carrier frequency of the pulse. The nonlinear parameter is defined as $\gamma = n_2\omega_0/cA_{eff}$, where n_2 is nonlinear-index coefficient and A_{eff} is the effective mode area. The left-hand side of Eq. 1 represents the linear terms and the

right-hand side represents nonlinear terms. The first moment of the nonlinear response function is defined as

$$R(t) = (1 - f_R)\delta(t) + f_R h_R(t) \tag{4.2}$$

where f_R, that be estimated to be about 0.18, represents the fractional contribution of the delayed Raman response to nonlinear polarization P_{NL}, $\delta(t)$ represents the delta function and h_R represents the Raman response function. In view of the damped oscillations, a useful form is

$$h_R(t) = \frac{\tau_1^2 + \tau_2^2}{\tau_1 \tau_2^2} \exp(-t/\tau_2) \sin(t/\tau_1) \tag{4.3}$$

where τ_1=12.2 fs, τ_2=32 fs.

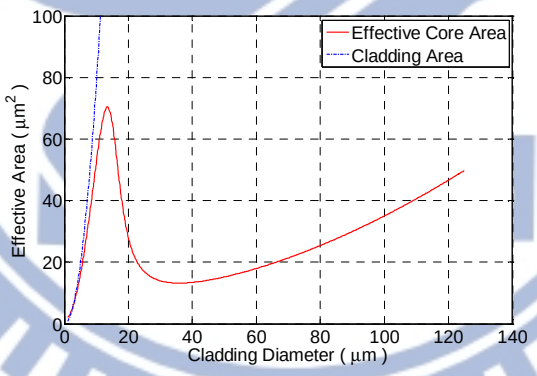

(a)

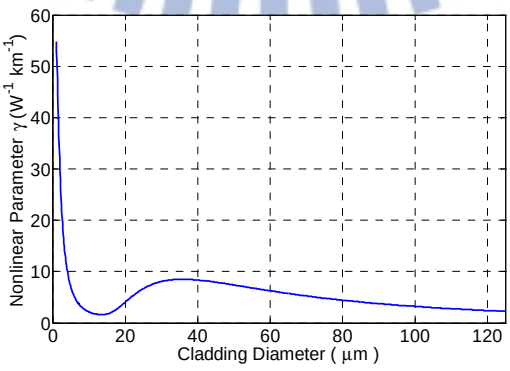

(b)

Fig. 4-4. (a) Effective mode area and (b) nonlinear parameter versus the waist of the tapered fiber at 830 nm.

We used symmetrized split-step Fourier algorithm to solve this nonlinear system numerically. The waist region of the tapered fiber is 10-mm-long with a uniform diameter of 1-μm. The transition region is 45 mm at each side. The fiber parameters adopt Corning SMF-28 specification. The effective core area A_{eff} is given by

$$A_{eff} = \frac{2\pi \cdot \left(\int_0^\infty r \cdot |F(r)|^2 \, dr \right)^2}{\int_0^\infty r \cdot |F(r)|^4 \, dr} \tag{4.4}$$

where $F(r)$ is the amplitude of the electric field for the fundamental mode at a radius r from the axis of the fiber. In our simulation, A_{eff} and nonlinear parameter γ is individually plotted against the diameter of the tapered fiber at the wavelength of 830 nm, as shown in Figs. 4-4(a) and (b). The A_{eff} is getting smaller as the cladding being thinner when the fiber diameter is larger than 35.8 μm; at this region the power is confined by the fiber core. However, the tapered fiber being thinner than 35.8 μm, the core leaves a large amount of light guided outside the core and the A_{eff} begins to increase until the diameter becomes 13.4 μm. When the power is guided by cladding-air interface, A_{eff} decreases rapidly as the fiber diameter. As the fiber diameter being getting thinner from 125 μm, 35.8 μm to 13.4 μm, the nonlinear parameter γ is from 2.254 W^{-1} km^{-1} increased to 8.507 W^{-1} km^{-1} and than decreased to 1.595 W^{-1} km^{-1}. Note the diameter of tapered fiber being 13.4 μm has smaller nonlinear parameter than untapered fiber. The nonlinear parameter increases rapidly as the fiber diameter thinner than 13.4 μm. Finally, the 1 μm-diameter waist area, the nonlinear parameter γ is 54.86 $W^{-1}km^{-1}$ which is approximately 25 times larger than that at the untapered region, thus exhibits large nonlinear effects to contribute to intense nonlinear processes.

The refractive index of the standard single-mode fiber is obtained using Sellmeier formula, and the propagation constant β is derived by solving the eigen-value equation. Expand β in a Taylor series about the pump frequency that obtain the n-order dispersion coefficients. The zero-, first, second, and third order dispersion coefficients β_j are plotted in Figs. 4-5(a)-(d). At the waist region, negative second dispersion coefficient ($\beta_2<0$) denote anomalous dispersion, which favors soliton formation and also benefits generation of octave-spanning white light. However, the β_2 is positive when the fiber diameter is larger than 2.6 μm, and becomes negative with the zero dispersion cross point located at the fiber diameter being 2.6 μm, as can be seen from Fig. 4-5(c). The β_2 has maximum value when the fiber diameter is 11.5 μm. This dispersion variation indicates pulse propagation behavior can be greatly influenced by the sign of the dispersion in the transition region of the tapered fiber, which will be discussed in the next section.

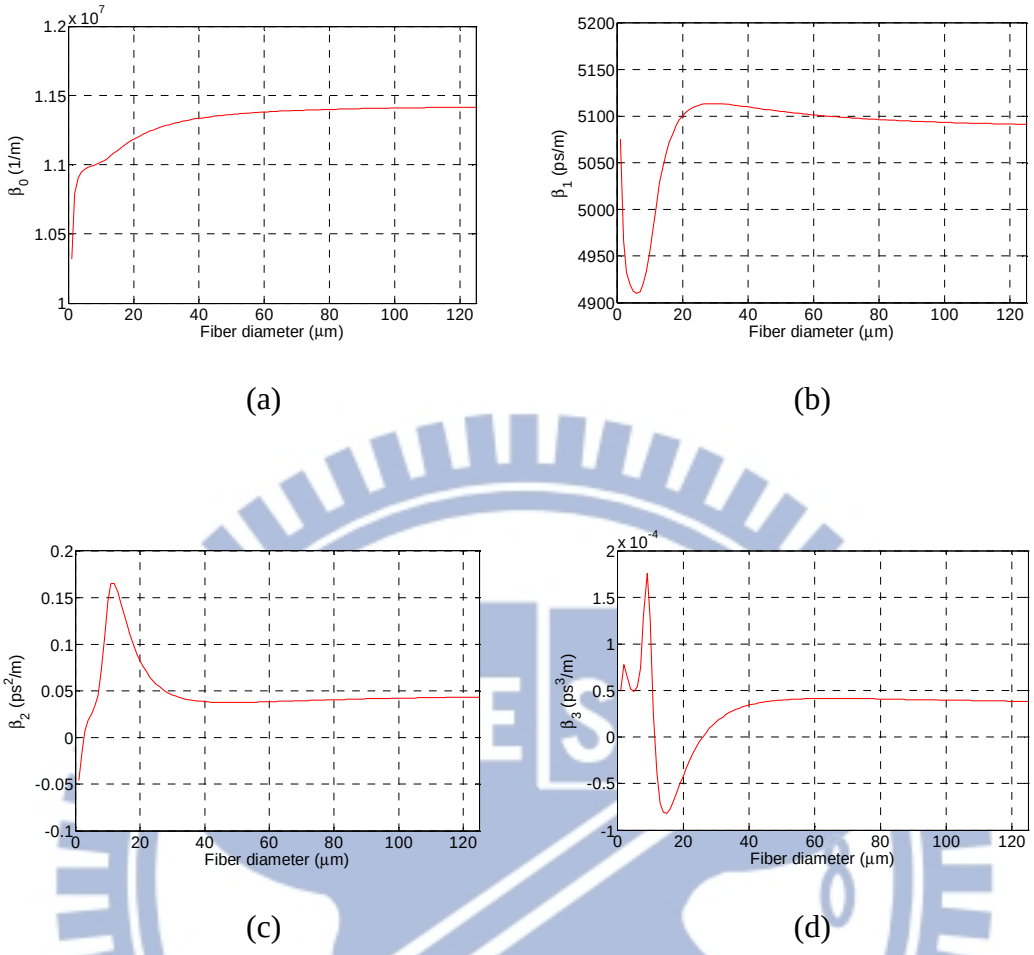

Fig. 4-5. (a)-(d) the dispersion coefficients versus the diameter of the tapered fiber at 830 nm.

Figures 4-6 show the simulation results of supercontinuum spectra for light propagates in the tapered fiber under different average powers using the hyperbolic secant pulses with a center wavelength of 830nm and repetition rate of 82 MHz. Owing to the inaccuracy measured the geometric parameters of the tapered fiber and the coupling efficiency of the entire tapered fiber, there are slightly different between the simulation results and experiment results. However, the generated spectra broadens when the launch power increases, and the long wavelength grows faster than the short wavelength region, which agrees well with the experimental observation as shown in Fig. 4-6. The spectral bandwidth $\Delta\lambda$ defined at the detuning wavelength

with intensity of -20 dB to that at peak wavelength is around 180 nm at 400 mW input power in the simulation result, which agrees well with the experimental results in Fig. 4-6.

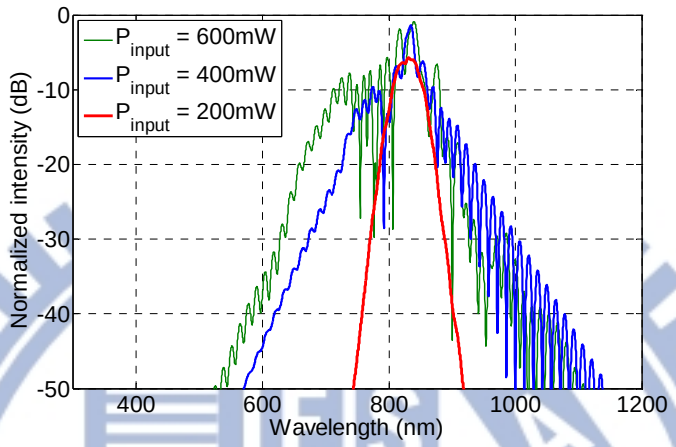

Fig 4-6. Simulation results of generated spectra at different pump powers using 1-μm-diameter fiber tapers with different launched pump powers.

The evolutions of the spectral intensity and the time domain pulse shape along the whole region of the tapered fiber are plotted in Fig. 4-7 for investigating the processes of the supercontinuum generation. The color from red to blue represents the intensity from strong to weak and the vertical white lines denote the boundary of the waist region. During the input transition region, the spectrum is slightly broadening but the time domain pulse shape is broadening obviously consequent on the interaction of the linear dispersion. The spectrum spread quickly in the waist region where the nonlinearity is 25 times larger than that at the untapered region and the stimulated Raman scattering play significant roles therefore its spectrum is asymmetrical. In the time domain, the pulse width gradually narrows in the waist region because of anomalous dispersion; however in the end of the waist region the pulse is splitting from the nonlinearity and anomalous dispersion interaction. In the

subsequent output transition region, the pulse split into several group when the transition region is in anomalous dispersion regime; however, those sub-pulse cross the zero dispersion point and reach normal dispersion regime, they broaden with propagation direction.

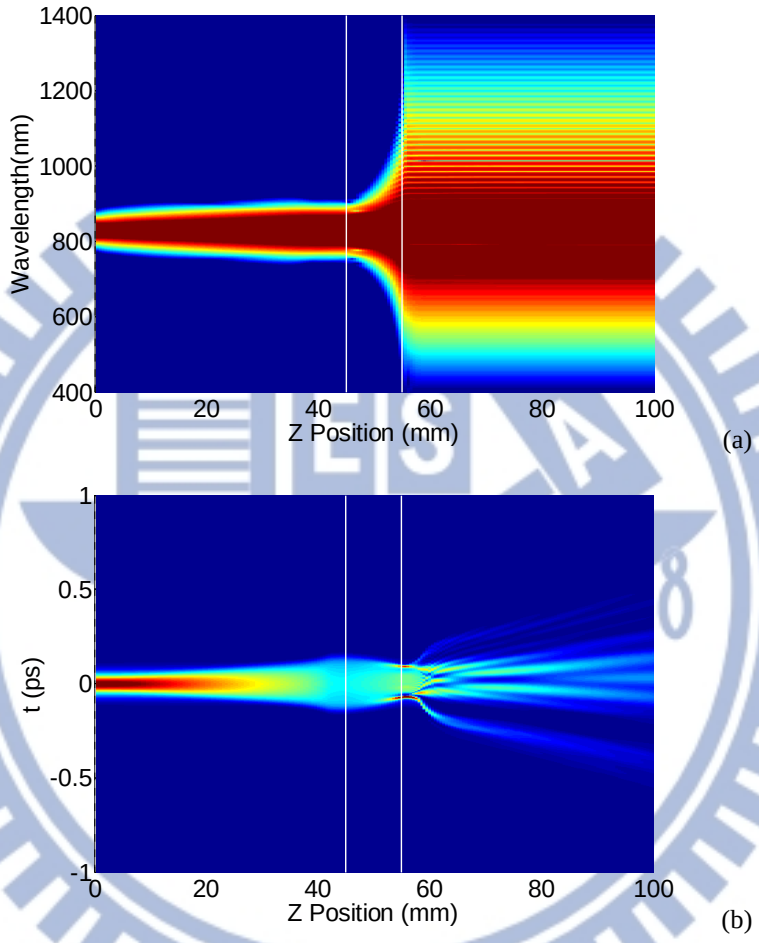

Fig. 4-7. Simulation results of (a) the spectrum evolved along the tapered fiber and (b) the time domain pulse evolved along the tapered fiber, that the input average power is 400 mW.

Many previous studies assume that the effect of nonlinearity in taper transition region is much smaller than that in the waist region, thus it can be neglected when the numerical simulation is performed. However, according to our result of numerical simulation, the nonlinear effect in taper transition region apparently influences the spectral broadening so that it cannot be ignore. The red line in Fig. 4-8(a) accounts

both the linear and nonlinear effect in the transition of the taper fiber, while the blue line represents the numerical result considering only the nonlinear effect in the taper transition region. According to Fig. 4-8, the effect of nonlinearity narrows the spectral broadening range and suppresses the blue-shift. To analyze the importance of the nonlinear effect in taper transition region in another viewpoint, the induced frequency chirp when the pulse propagates through the first taper transition region is calculated, as shown in Fig. 4-8(b). Due to the normal-dispersion regime in the taper transition region, the frequency chirp induced by the nonlinear effect and the linear dispersion cannot cancel each other, on the contrary, spectral broadening range degrades as a result of the frequency chirp enhancement due to the nonlinear effect. The pulse shape in time domain is displayed in Fig. 4-8(c). The nonlinear effect in taper transition region broadens the pulse width since the individual frequency chirp induced by the normal-dispersion and the nonlinear effect has the same sign. The broaden pulse width at the exit of the first taper transition lowers the capacity of the supercontinuum generation when the pulse propagates along the following waist region.

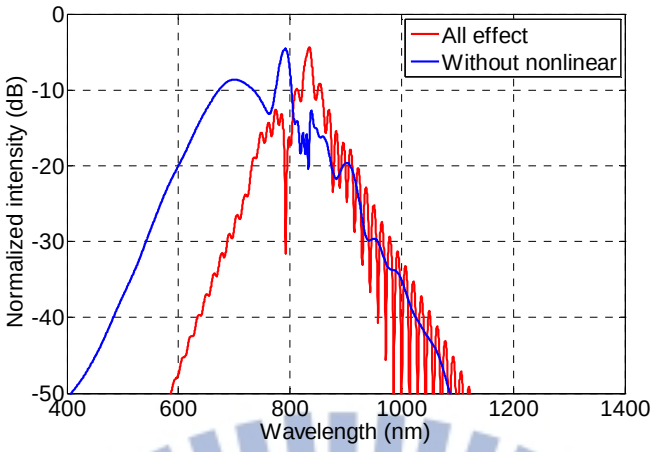

(a)

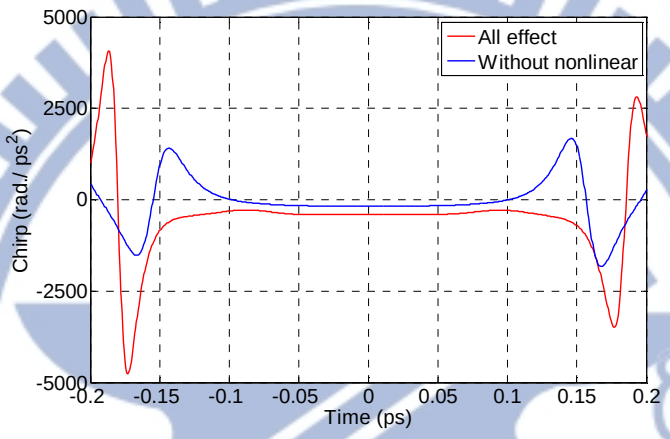

(b)

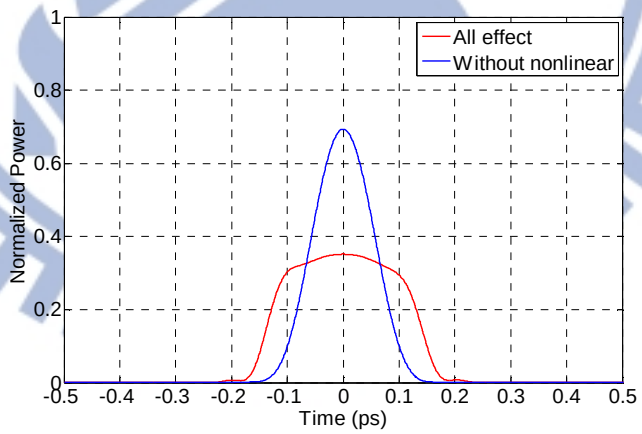

(c)

Fig. 4-8. (a)Spectral broadening, (b)frequency chirp when pulse launching into the fiber waist, (c)time domain pulse shape when pulse launching into the fiber waist for comparison between the nonlinear effect being neglected and considered.

Two different shapes of taper transition region are further considered to

investigate the influence on supercontinuum generation. Assume the shape of the fiber taper is linear tapered and exponential tapered, and the calculated broadening spectra are respectively shown in Fig. 4-9(a). The blue line presents the linear tapered shape, while the red line shown the exponential tapered shape. It can be shown in the Figure that the spectral broadening for linear tapered shape is narrower than that of the exponential tapered shape. The corresponding frequency chirp and pulse width in time-domain when the pulse propagates through these two different shapes of taper transition region are shown in Figs. 4-9(b) and 4-9(c). Owning to different shapes of taper fiber, the amount and ratio of normal-dispersion, anomalous-dispersion, and nonlinear effect slightly vary when pulse propagates in taper transition region. The exponential tapered shape contains the larger pulse width and lower peak power than that of the linear tapered shape, therefore, the supercontinuum generation efficiency decreases when propagating in the following waist region.

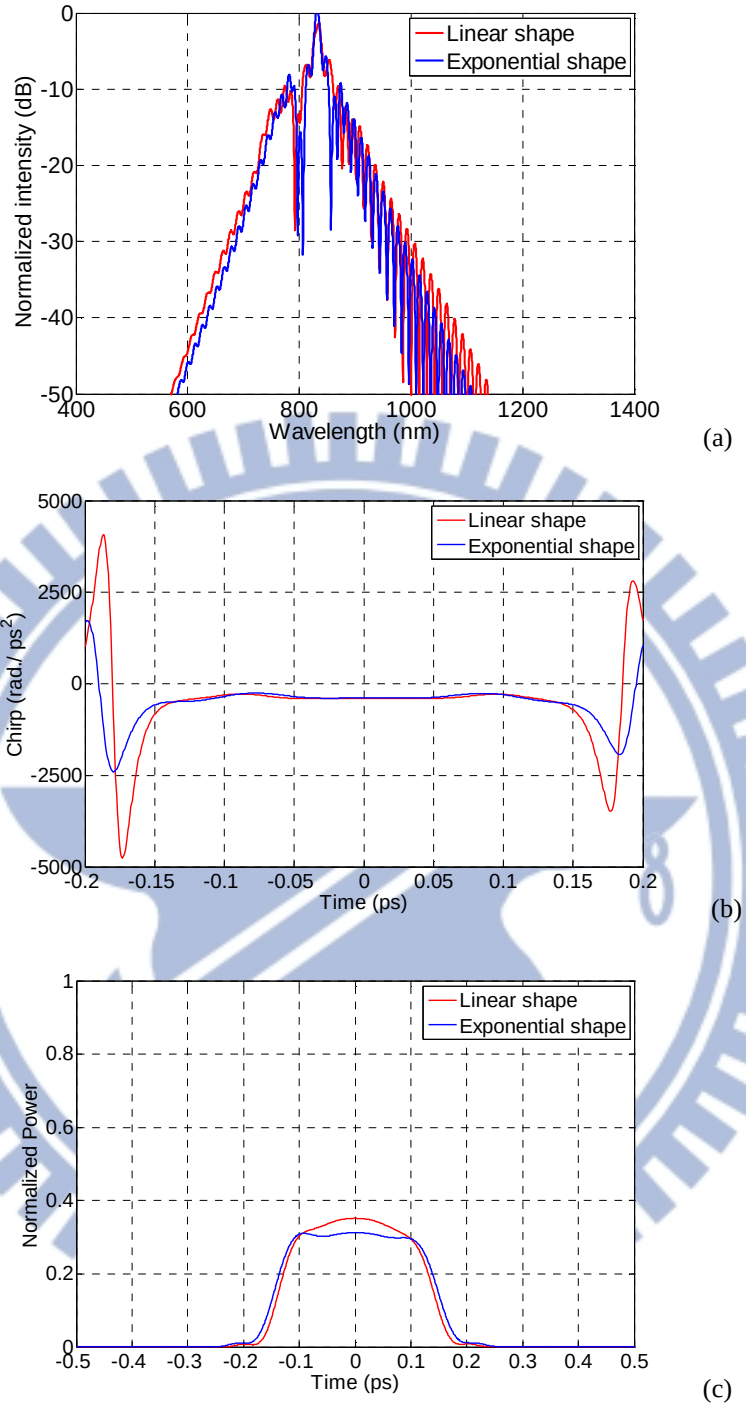

Fig. 4-9. (a)Spectral broadening, (b)frequency chirp when pulse launching into the fiber waist under different shapes of the fiber taper.

From above discussion, the amount of frequency chirp of the pulse when it launches into the fiber waist can greatly change the supercontinuum generation spectrum. Therefore, the normalized optical field associated with incident pulse takes

the form

$$U(0,T) = \sec h\left(\frac{T}{T_0}\right)\exp\left(-\frac{iCT^2}{2T_0^2}\right), \tag{4.5}$$

The dispersion effect in fiber taper is too complicated to totally compensate by simply adopting conventional dispersion compensation methods. However, the adjustment on the value C can partially compensate the pulse broadening result due to the pulse propagation in taper transition. Figure 4-10(a) presents the supercontinuum generation result using a chirped pulse with C=-1 launched into the fiber taper. The red line in Fig. 4-10(a) is the result for launching an unchirped pulse, and the blue line is the chirped pulse. The spectral broadening range is wider and the efficiency of supercontinuum generation if higher for launching an unchirped pulse rather than launching a chirped pulse. Figures 4-10(b) and 4-10(c) individually plot the frequency chirp and the pulse width in time domain corresponding to a chirp and an unchirp pulse propagation the input of the fiber waist. Because the pulse propagates in the first taper transition experiences mainly normal-dispersion (β_2>0), the initially pulse-width narrowing stage in time domain can be observed for the propagation of the chirped pulse with C=-1.

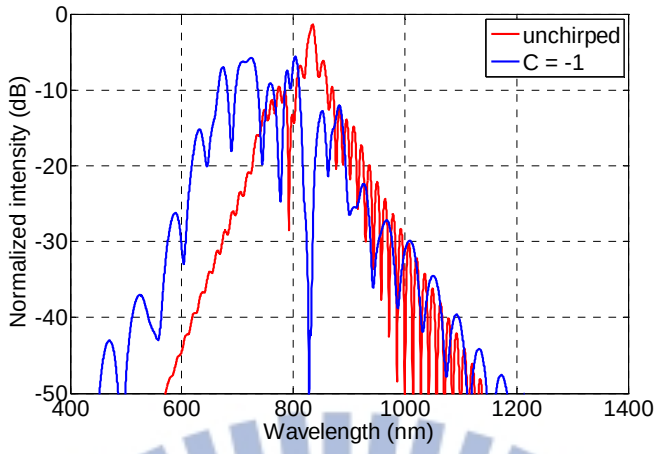

(a)

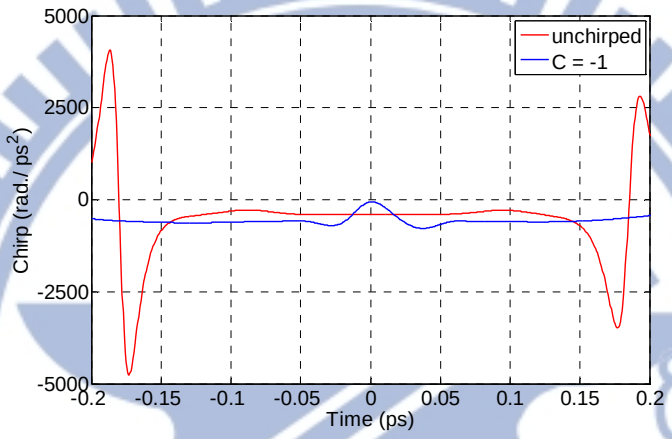

(b)

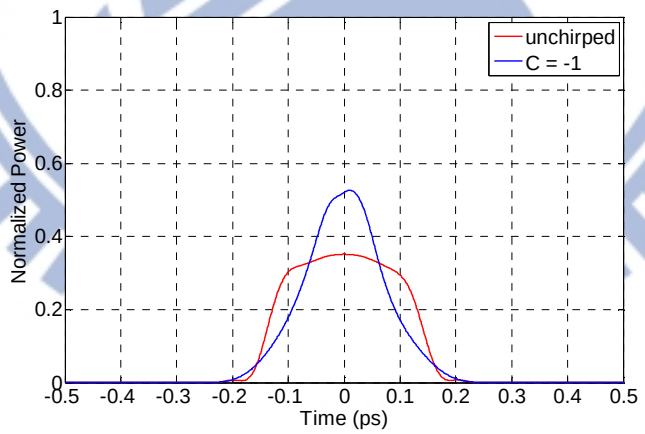

(c)

Fig. 4-10. (a)Spectral broadening, (b)frequency chirp when pulse launching into the fiber waist (c)time domain pulse shape when pulse launching into the fiber waist for chirped and unchirped pulse.

4.4 Conclusions

Supercontinuum generation from 1-μm tapered fiber using the 80 fs Ti:sapphire laser excitation is demonstrated experimentally and studied theoretically. By properly choosing the exciting wavelength, relatively wide spectra is observed from near UV to near IR only using 1-cm long and 1-μm-diameter optical tapered fiber. Besides, exciting power can be greatly lower down for wide spectra generation extended to near UV by properly connecting two fiber tapers. Split-step FFT method is investigated numerically in order to analyze the spectral response of supercontinuum generation phenomenon corresponding to the wavelength dependent loss occurred at transition region of the tapered fiber. The simulation results agree with the experimental results, and shows that the dispersion and nonlinear effects at transition region of the tapered fiber greatly influences the broaden spectrum shape. The theoretical result indicates that the zero dispersion cross point located at 2.6 μm so that the pulse width and peak power of the excited pulse is dramatically changed when propagates in transition region, which in term apparently affects the supercontinuum generation spectrum. Hopefully the simulation results in this work provide a helpful viewpoint to analyze the supercontinuum generation in typical tapered fibers.

References

[1] G. Genty, S. Coen, and J. M. Dudley, "Fiber supercontinuum sources," *J. Opt. Soc. Am. B*, vol. 24, 1771, (2007).

[2] J. K. Ranka, R. S. Windeler, and A. J. Stentz, "Visible continuum generation in air-silica microstructure optical fibers with anomalous dispersion at 800 nm," *Opt. Lett.*, vol. 25, 25, (2000).

[3] J.-H. Lin, C.-C. Hsu, W.-F. Hsieh, and K.-H. Lin, "Build-up of supercontinuum in heated and unheated photonic crystal fibers using a chirped femtosecond laser," *Opt. Commun*., vol. 265, 659 (2006).

[4] R. Buczynski, D. Pysz, T. Martynkien, D. Lorenc, I. Kujawa, T. Nasilowski, F. Berghmans, H. Thienpont, and R. Stepien, "Ultra flat supercontinuum generation in silicate dual core microstructured fiber," *Laser Phys. Lett.*, vol. 6, 575, (2009).

[5] R. R. Gattass, G. T. Svacha, L. Tong, and E. Mazur, "Supercontinuum generation in submicrometer siameter silica fibers," *Opt. Express*, vol. 14, 9408, (2006).

[6] M. A. Foster, A. C. Turner, M. Lipson, and A. L. Gaeta, "Nonlinear optics in photonic nanowires," *Opt. Express*, vol. 16, 1300, (2008).

[7] G. Genty, B. Kibler, P. Kinsler, and J. M. Dudley, Opt. Express 16, "Harmonic extended supercontinuum generation and carrier envelope phase dependent spectral broadening in silica nanowires," *Opt. Express*, vol. 16, 10886, (2008).

[8] W. Ding, C. Benton, A. V. Gorbach, W. J. Wadsworth, J. C. Knight, D. V. Skryabin, M. Gnan, M. Sorrel, and R. M. De La Rue, "Soliton and spectral broadening in long silicon-on-insulator photonic wires," *Opt. Express*, vol. 16, 3310, (2008).

[9] M. Lamont, B. Luther-Davies, D. Choi, S. Madden, and B. J. Eggleton, "Supercontinuum generation in dispersion engineered highly nonlinear (γ=10/W/m) As2S3 chalcogenide planar waveguide, *Opt. Express*, vol. 16, 14938,

(2008).

[10] M. Ferrera, L. Razzari, D. Duchesne, R. Morandotti, Z. Yang, M. Liscidini, J. E. Sipe, S. Chu, B. E. Little, and D. J. Moss, “Low-power continuous-wave nonlinear optics in doped silica glass integrated waveguide structures,” *Nature Photonics*, vol. 2, 737, (2008).

[11] T. A. Birks, W. J. Wadsworth, and P. St. J. Russell, “Supercontinuum generation in tapered fibers,” *Opt. Lett.*, vol. 25, 1415, (2000).

[12] J. Teipel, K. Franke, D. Türke, F. Warken, D. Meiser, M. Leuschner, and H. Giessen, “Characteristic of supercontinuum generation in tapered fibers using femtosecond laser pulse,” *Appl. Phys. B*, vol. 77, 245, (2003).

[13] R. Zhang, X. Zhang, D. Meiser, and H. Giessen, “Modal and group velocity dispersion evolution in the tapered region of a single-mode tapered fiber,” *Opt. Express*, vol. 12, 5840, (2004).

[14] D. Türke, S. Pricking, A. Husakou, J. Teipel, J. Herrmann, and H. Giessen, “Coherence of subsequent supercontinuum pulses generated in tapered fibers in the femtosecond regime,” *Opt. Express*, vol. 15, 2732, (2007).

[15] R. Zhang, X. Zhang, D. Meiser, and H. Geissen, “Mode and group velocity dispersion evolution in the tapered region of a single-mode tapered fiber,” Opt. Express 12, 5840 (2004).

[16] Z. Wang, H. Sone, Y. Tsuji, and M. Imai, “Spectral Phase and Intensity Evolutions of Supercontinuum Generation in a Biconical Tapered Fiber,” *Opt. Rev.*, vol. 14, 81, (2007).

[17] J. M. Dudley and S. Coen, “Numerical Simulations and Coherence Properties of Supercontinuum Generation in Photonic Crystal and Tapered Optical Fibers,” *IEEE J. Sel. Top. Quantum Electron.*, vol. 8, 651, (2002).

[18] M. Kolesik, E. M. Wright, and J. V. Monloney, “Numerical Simulations and Coherence Properties of Supercontinuum Generation in Photonic Crystal and Tapered Optical Fibers,” *Appl. Phys. B*, vol. 79, 293, (2004).

[19] S.-Y. Chou, K.-C. Hsu, N.-K. Chen, S.-K. Liaw, Y.-S. Chih, Y. Lai, and S. Chi, “Analysis of thermo-optic tunable dispersion-engineered short-wavelength-pass tapered-fiber filters,” *J. Lightwave Technol.*, vol. 27, 2208, (2009).

[20] K.-C. Hsu, N.-K. Chen, S.-Y. Chou, S.-K. Liaw, Y. Lai, and S. Chi, “Bandpass Filter with Variable Bandwidth based on Tapered Fiber with External Polymer Cladding,” *IEEE Photon. Technol. Lett.*, vol. 21, 935 (2009).

Chapter 5

The Stable and Tunable Fiber Laser

5.1 Introduction

Single-longitudinal-mode (SLM) Erbium-doped fiber (EDF) ring lasers have potential applications in optical communications, fiber sensors, and spectroscopy. In accordance with these Erbium fiber lasers, the unidirectional ring-cavity structure, which can potentially offer more output power with low relative intensity noise, has been extensively studied [1] – [4]. Due to the requirements of intracavity components and connecting fibers, a rather long cavity length of the fiber ring laser is unavoidable and brings out an enormous number of densely spaced longitudinal modes lying beneath the Erbium gain curve. To complete single-longitudinal-mode operation, several single-longitudinal-mode fiber lasers techniques have proposed, such as using two cascaded Fabry-Perot filters into the ring cavity [5], employing a compound ring resonator composed of a dual-coupler fiber ring and a tunable bandpass filter (TBF) [6], and utilizing twisted EDFs and fiber-type half-wave plate to control the cavity [7], [8].

In this chapter, I propose and investigate experimentally a sable and tunable fiber double-ring laser to achieve single-longitudinal-mode operation, based on an Erbium-doped waveguide amplifier (EDWA), a fiber Fabry-Perot tunable filter (FFPTF), and a polarization controller into the ring cavity. Moreover, the output

power, side-mode suppression ratio (SMSR), and the stabilities of power and wavelength of the laser are also discussed.

5.2 Experiments and Results

Fig. 5-1 illustrates the proposed single-longitudinal-mode Erbium-doped fiber double-ring laser. The proposed architecture consists of an EDWA, two 3 dB optical couplers (OCPs), a fiber Fabry-Perot tunable filter (FFB-TF), and a polarization controller (PC). The EDWA, which is manufactured via twostep ion-exchange process, has the advantage of inheriting the known properties of the Erbium-doped fiber amplifier (EDFA), such as low noise figure, slight polarization dependence, and no crosstalk between wavelength-divisionmultiplexing (WDM) channels. All optical performances are measured when the laser pump diode current equals to 440 mA at ambient temperature. The polarization controller is used to align the state of polarization of the ring cavity to guarantee a stable oscillation. The FFP-TF is an all-fiber device having a widely tunable range, low insertion loss of < 0.5 dB, and low polarization-dependent loss of ~ 0.1 dB. This FFP-TF having the free spectral range (FSR) of 44 nm can provide wavelength selection in the ring laser cavity by controlling the external voltage (0 to 12 V) on the piezoelectric transducer (PZT) of this filter. In addition, an optical spectrum analyzer (OSA) with a 0.05 nm resolution is used to measure the output spectra of ring laser.

The FFP-TF not only determines a lasing wavelength but also serves as a mode-restricting component to provide the first restriction on the possible laser modes. Because of the combination of a FFP-TF and a double-ring cavity, a single-longitudinal-mode operation in this fiber laser is achieved. The wavelength

mode oscillates only at a single frequency, which satisfies the resonant conditions of the proposed structure.

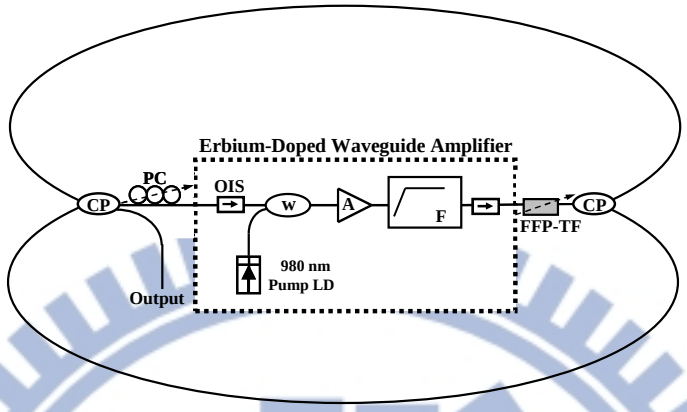

Fig. 5-1 Proposed fiber double-ring laser architecture for SLM operation

The cavity of ring laser has a free spectral ranges (FSRs), FSR = c/nL, where c is the speed of light in vacuum, n is the average refractive index of the singlemode fiber of 1.468 and L is the total cavity length. The proposed ring laser has two ring cavities, as shown in Fig. 5-1. In this experiment, the two ring lengths of 11.96 and 13.04 m are the optimal choice for single-longitudinal-mode operation. Therefore, the lengths of two ring loops are 11.96 and 13.04 m long, corresponding to the FSRs of nearly 17.1 and 15.7 MHz, respectively. Then, the single-frequency operation of the fiber laser and its influence can be verified by a self-homodyne detection method. An optical circuit for a measurement is composed of a photodetector with a 3 dB bandwidth of 12 GHz and a Mach-Zehnder interferometer with a 25 km long standard single-mode fiber (SMF).

Fig. 5-2 illustrates the output wavelengths of the proposed fiber laser in an operating range of 1530 to 1560 nm. Fig. 5-2 also shows that all the output side-mode suppression ratios are above 64.6 dB. To realize the output behaviors of the laser, Fig. 5-3 shows the output power and side-mode suppression ratio versus different

wavelength for the proposed laser over the wavelengths of 1530 to 1560 nm. Fig. 5-3 presents that the output power and side-mode suppression ratio of the laser are large than −5 dBm and 64.6 dB at 1550 nm in the effectively operating range. The maximum output power and side-mode suppression ratio (SMSR) of the laser are 4.3 dBm and 70.2 dB at 1536 nm, as also seen in Fig. 5-3. Compared with the past report [9], the proposed laser has the lower cost and simpler scheme. Moreover, the side-mode suppression ratio of the proposed laser is better (minimal SMSR of > 64.6 dB) than that of [9] (minimal SMSR of > 30 dB). Therefore, the proposed fiber laser not only has easily structure but also has better performance compared with the past.

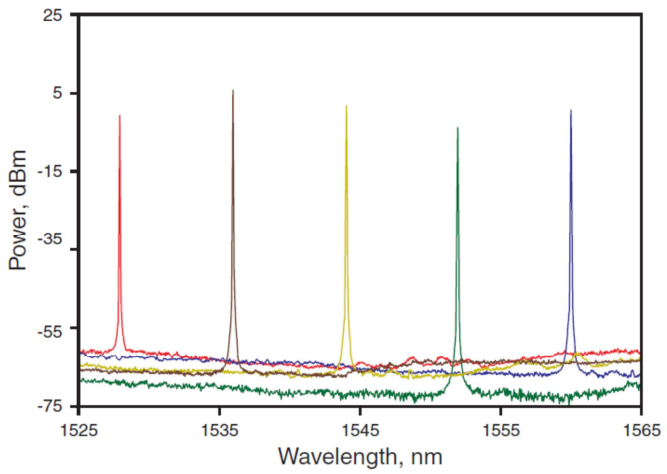

Fig. 5-2 Output wavelengths of the proposed fiber laser in an operating range of 1530 to 1560 nm.

In order to investigate the performance of output power and wavelength, a short-term stability of the laser is measured in Fig. 5-4. An initial lasing wavelength is set at 1546.5 nm and total observing time is over 60 minutes. The results show that our proposed fiber laser has an excellent performance. The output power and central wavelength variations are less than 1 dB and 0.04 nm, respectively.

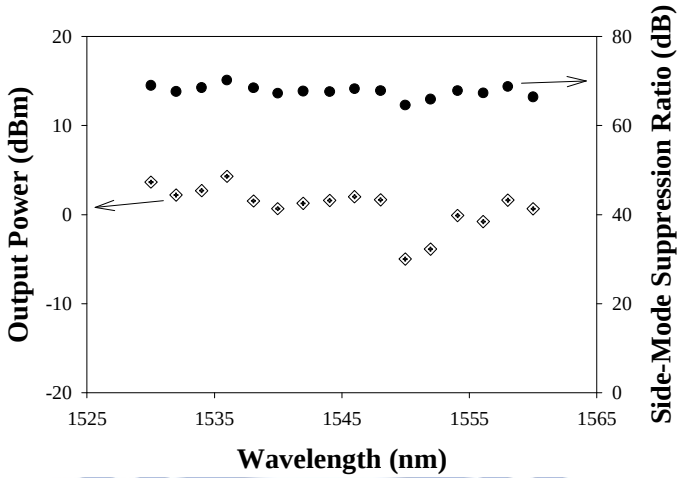

Fig. 5-3 Output power and SMSR versus different wavelength for the proposed laser over the wavelengths of 1530 to 1560 nm

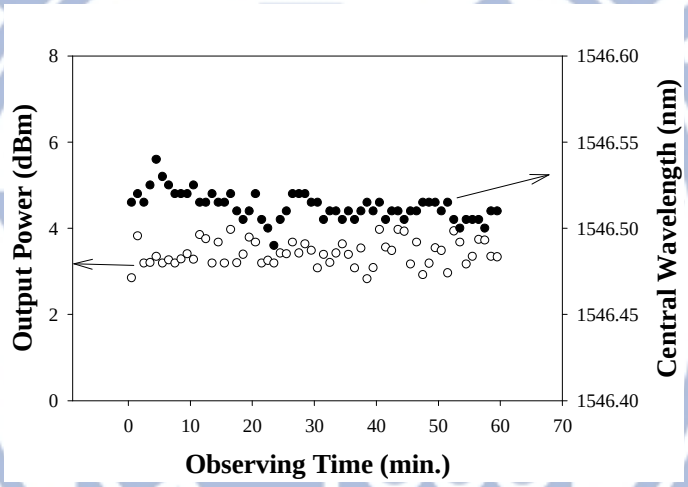

Fig. 5-4 Output wavelength and power variations of the proposed laser for a lasing wavelength of 1546.5 nm initially and an observing time of 60 minutes

To verify the single-frequency performance, the self-homodyne spectra of the fiber laser without and with double-ring structure (an operating wavelength is at 1546.5 nm) as shown in Fig. 5-5a and Fig. 5-5b, respectively. A noisy and unstable waveform with spikes is observed in the spectrum of single-ring laser as seen in Fig. 5-5a. When it is combined with a double-ring configuration, the proposed resonator can guarantee a single-longitudinal-mode laser oscillation in Fig. 5-5b. Simultaneously, the fiber laser effectively suppresses sidemode frequencies of 500

MHz, also shown in Fig. 5-5b.

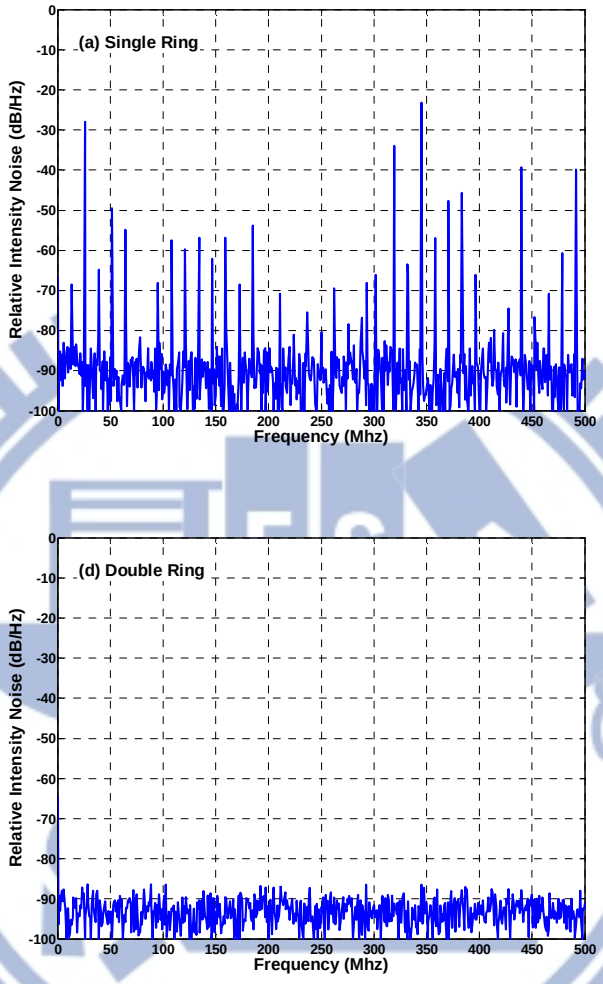

Fig. 5-5 Self-homodyne spectra of the (a) single-ring and (b) double-ring laser at 1546.5 nm initially

5.3 Conclusion

This chapter has proposed and investigates experimentally a tunable and stable fiber laser with single-longitudinal-mode output based on double-ring architecture. Double-ring structure provides a fine mode restriction and guarantees a

single-longitudinal-mode operation. The output power of larger than −5 dBm and the side-mode suppression ratio of larger than 64.6 dB over the operating range from 1530 to 1560 nm can be obtained. And the maximum output power and side-mode suppression ratio of the laser are 4.3 dBm and 70.2 dB at 1536 nm. In addition, the power fluctuation of less than 1 dB and the central wavelength variation of less than 0.04 nm also are observed for lasing wavelength in a short-term observing time.

References

[1] K. K. Chow, C. Shu, M. W. K. Mak, and H. K. Tsang, “Widely tunable wavelength converter using a double-ring fiber laser with a semiconductor optical amplifier,” *IEEE Photon. Technol. Lett.*, vol. 14, 1445, (2002).

[2] R. M. Sova, K. Chang-Seok, J. U. Kang, and J. B. Khurgin, “Tunable dual-λ fiber ring laser based on 2nd order Sagnac-Lyot fiber filter,” *IEEE CLEO 2002 Tech. Dig., USA 2002*, vol. 1, 444, (2002).

[3] H. Ahmad, N. K. Saat, and S. W. Harun, “S-band erbium-doped fiber ring laser using a fiber Bragg grating,” *Laser Phys. Lett.*, vol. 2, 369, (2005).

[4] F. Abdullah, A.S.M. Noor, M.A. Mahdi, H.A.A. Rashid, and M.K. Abdullah, “Intracavity loss control effect on tuning range of tunable dual erbium-doped fiber laser,” *Laser Phys. Lett.*, vol. 2, 535, (2005).

[5] K.J. Vahala, P. Namkyoo, J. Dawson, and S. Sanders, “Tunable, single-frequency, erbium fiber ring lasers,” *Proc. IEEE LEOS 1993 Conf., USA 1993*, 708, (1993).

[6] G.A. Ball, W.W. Morey, and W.H. Glenn, “Standing-wave monomode erbium fiber laser,” *IEEE Photon. Technol. Lett.*, vol. 3, 613, (1991).

[7] V. Mizrahi, D.J. Digiovanni, R.M. Atkins, S.G. Grubb, Y.K. Park, and J.M.P. Delavaux, “Stable single-mode erbium fiber-grating laser for digital communication,” *J. Lightwave Technol.*, vol. 11, 2021, (1993).

[8] J. Zhang, C.Y. Yue, G.W. Schinn, W.R.L. Clements, and J.W.Y. Lit, “Stable sinlge-mode compound-ring erbium-doped fiber laser,” *J. Lightwave Technol.*, vol. 14, 104, (1996).

[9] H.C. Chien, C.H. Yeh, C.C. Lee, and S. Chi, “A tunable and single-frequency S-band erbium fiber laser with satyrable-absorber-based autotracking filter,” *Opt. Commun.*, vol. 250, 163, (2005).

Chapter 6

Projection Moiré Profilometry with High-Dynamic Range Image

6.1 Introduction

Accurately measuring the 3-D shapes of the objects is important for the industry to speed up the product development and ensure the manufacturing quality. In general, the techniques of 3-D shape measurement can be classified into two categories: contact-surface measurement and noncontact-surface measurement. The contact-surface techniques can provide the high accuracy for the measurement of any "hard" objects which are insensitive to the optical properties of the surface. However, there are risks for the contact-surface techniques to damage the surface of the object inspected. Moreover, as a point-by-point measuring technique, the speed of the contact-surface technique is usually very slow. In contrast, the noncontact-surface methods would not damage the surface of the object inspected. Although among these two types of techniques different optical methods are extensively adopted, it is still an exceptional challenge for an object tested in an optical inspection system with a wide range of variation of the surface reflectivity. In addition, for increasing the speed of the measurement, the image detectors with low dynamic range are utilized typically providing 8 bits of brightness data only for each pixel. Hence the image captured by

the imaging system ends up being too dark in some areas and possibly being saturated in others. Since the optical signal of the measuring region cannot be properly retrieved, these inspection methods would result in the loss of its accuracy.

An overview of 3-D shape measurement using various optical methods was provided by Chen [1]. The merits of the structured light method, also categorized as active triangulation, are (1) easy implementation, (2) fast full-field measurement, and (3) phase shifting with the fringe density and the direction change implemented without moving parts if a computer-controlled LCoS / DLP is used [2-4]. However, the optical properties of the object surface would affect the accuracy and thus a variety of optical 3-D shape measurement methods had been proposed for the shiny surfaces [5-6]. Nevertheless, for the object with very high dynamic range of its surface reflectivity, all these proposed methods might be potentially problematic. Zhang and his coauthors addressed a high dynamic range (HDR) technique to measure this type of object [7]. They reported that multiple shots of the fringe images with different exposures were taken for each measurement. The final fringe images, used for phase retrieval, were produced pixel-by-pixel by choosing the brightest but unsaturated corresponding pixel form one shot. A phase-shifting algorithm was employed for computing the phase that can be further converted to 3D coordinates. Therefore, the multiple shots taken can overcome the very high dynamic range of surface reflectivity; but it is oppositely a time-consuming measurement. On the other hand, Nayar suggested that using an optical mask adjacent to a conventional image detector array can achieve a high dynamic range image detector [8]. On the mask there was a pattern with the spatially varying transmittance, thereby giving adjacent pixels on the detector the different exposures to the scene. The captured image was mapped to a high dynamic range image by using an efficient image reconstruction

algorithm; however, this method must downgrade spatially resolution for gaining a high dynamic range image.

In comparison with the previous studies, this chapter presents a technique for a low dynamic range imaging device, such as a CCD camera, to acquire a high dynamic range image in one-shot. Thereby, it is possible to measure a very wide range of the surface reflectivity without any reduction in the spatial resolution. The availability of the extra bits of the data at each image pixel enhances the robustness of the phase-retrieving algorithms so that an accurate surface topography of a measured object can be obtained. A digital-light-processing (DLP) is used as the light modulation for the control of the distribution of the light intensity when a sample is in higher reflectivity regions but under lower light illumination. The dull regions are illuminated with higher light intensity to produce a raw image whose surface brightness levels for all pixels are ranged within the dynamic range of a CCD camera. Thereafter, the single raw image is processed by a compensation operation according to an intensity gain ratio of the light intensity before and after being modulated by DLP. As a result, a high dynamic range image can be obtained from the low dynamic range imaging CCD. Since this system only requires its imaging device to capture one image for processing, the advantages are not only low time-consuming and low errors during multiple sampling but also high spatial resolutions. This proposed technique is not limited to 3-D shape measurement systems; it is applicable to any optical measurement techniques with variant spatial brightness.

6.2 Measurement Method

This work developed a projection moiré system for inspecting the high variation

range of surface reflectivity with the high speed measurement and preserving the spatial resolution. This system is based on a digital fringe projection and is associated with three-step phase-shifting algorithm. It retrieves the phase value of the fringe images and converts to 3-D shape. The basic configuration of the moiré system using digital fringe projection is shown in Fig. 6-1. A lamp is used for providing a uniform intensity distribution onto the DLP chip and then the modulated light is projected onto the object through a telecentric lens. The DLP chip controlled by a computer generates the fringe images which are projected onto the object under measuring. These fringe images are distorted and reflected by the object and then captured by a CCD camera. The DLP chip not only generates the fringe images for phase-shifting method but also adjusts the light intensity distribution to be ranged within the dynamic range of the CCD camera. Then a frame grabber, installed in the computer, acquires the digital fringe images through a camera-link interface. The computer processes the fringe images obtained to retrieve the phase by using both of the phase-shifting algorithm and the phase-unwrapping algorithm with further conversion to 3-D coordinates [9]. According to the three-step phase-shifting algorithm, the original projected fringe image intensities are presented as

$$I_1(x,y)=\alpha(x,y)+\beta(x,y)\cdot\cos\left[\varphi(x,y)-\frac{2\pi}{3}\right],$$

$$I_2(x,y)=\alpha(x,y)+\beta(x,y)\cdot\cos\left[\varphi(x,y)\right], \text{ and} \qquad (6.1)$$

$$I_3(x,y)=\alpha(x,y)+\beta(x,y)\cdot\cos\left[\varphi(x,y)+\frac{2\pi}{3}\right],$$

where α is the DC component or average intensity, β is the amplitude of the intensity modulation, and φ is the phase of the spatial modulation. The fringe image is reflected by the surface of the object under test and then is captured by the camera. Those fringe images actually captured by the camera are

$$I'_1(x,y) = r(x,y)\left\{\alpha(x,y) + \beta(x,y)\cdot\cos\left[\phi(x,y) - \frac{2\pi}{3}\right]\right\},$$

$$I'_2(x,y) = r(x,y)\left\{\alpha(x,y) + \beta(x,y)\cdot\cos\left[\phi(x,y)\right]\right\}, \text{ and} \qquad (6.2)$$

$$I'_3(x,y) = r(x,y)\left\{\alpha(x,y) + \beta(x,y)\cdot\cos\left[\phi(x,y) + \frac{2\pi}{3}\right]\right\},$$

where *r(x,y)* is related to the reflectivity of the object and the camera sensitivity. *(x,y)* is the phase of the fringe images after modulated by the object. The phase can be retrieved through Eq. (6.2) from Eq. (6.3)

$$\phi(x,y) = \tan^{-1}\left[\frac{\sqrt{3}\left(I'_1 - I'_3\right)}{2I'_2 - \left(I'_1 + I'_3\right)}\right]. \qquad (6.3)$$

The height of the object's surface is proportional to the phase difference, $\Delta\phi = \phi - \varphi$. The traditional method is on the basis of the constant average intensity (α) and the constant amplitude (β) of Eq. (6.1) for all field of view inside the measuring configuration. From Eq. (6.2), if a shiny region is within the field of view, the region presents large reflectivity and dominates both of the average intensity and the average amplitude. Consequently, with a possible shiny region it is necessary for traditional methods to pick up small average values of the intensity and the amplitude to avoid camera saturated. However, in general case the values are too small for some dull region to retrieve the phase from Eq. (6.3). By the point of view of mathematics, the intensity contrast could not affect the precision of the phase retrieved process; but the system is discrete and the small contrast will invoke large digitized noise during the phase retrieved process according to Eq. (6.3). This chapter presents a novel projection moiré system which could avoid contrast loss for inspecting the high variation range of surface reflectivity. The DLP chip not only adjusts the light intensity for the whole region but also adjusts the intensity pixel-by-pixel. The system

could optimize the average intensity and the average amplitude of each pixel. This function could ensure the whole region enough contrast gained for performing the phase retrieved process.

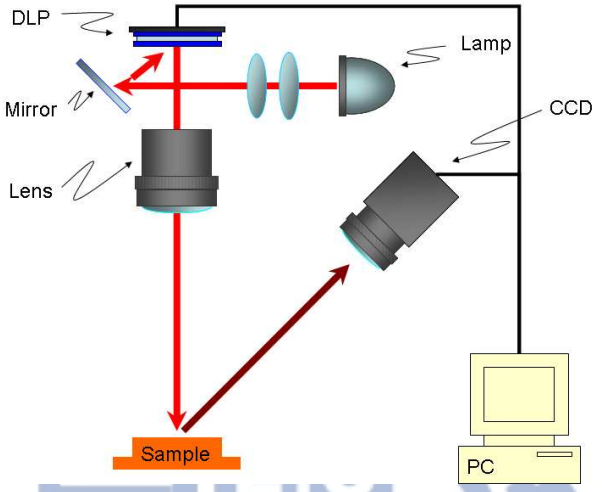

Fig. 6-1 The system configuration

In this study used Optoma EP728 DLP projector to create the signals of the fringe image with a resolution of 1024x768, and the fringe pitch was 3.3 mm (150 pixels). The camera that we used was SONY XCL5005 with a resolution of 2400x2014 and 12 bits/pixel. The frame grabber was DALSA X64 Xcelera-CL PX4 with a camera-link interface. The field of view in this system was 53x45 mm.

6.3 Results and Discussion

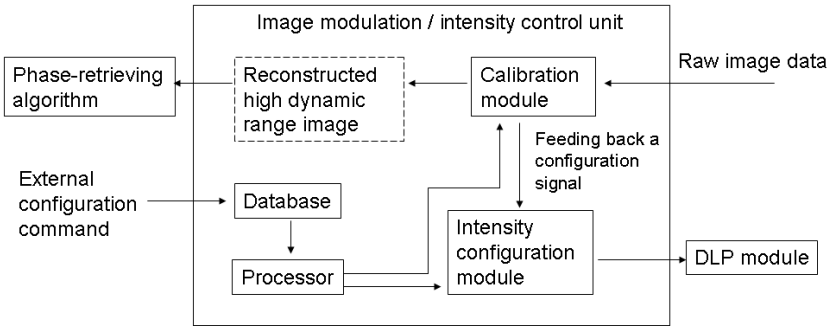

Fig. 6-2 The block diagram of a control unit

The block diagram of the intensity control unit is shown in Fig. 6-2. Firstly, Controlled the DLP to form uniform distribution of the light intensity and projected the light on the sample. Since there were shiny and dull regions on the surface of this sample, the image captured by the CCD ended up with dark in some areas and possibly with saturated in others. The calibration module received the raw image data from the CCD and an image processing algorithm indicated the boundary of the regions with different values of the surface reflectivity within the field of view and then resulted in the calibration factors for each region. The estimated factors were fed back to the intensity configuration module for the adjustment of the intensity of the fringe images and for the guarantee of the intensity of all regions being within the dynamic region of the CCD camera. For the industrial manufacturing process, the similar inspection condition would be assured that the boundary regions and calibration factors can be loaded from the database. For the phase-shifting algorithm, the modulated fringe images with the revision of the average intensity and the amplitude for different region from calibration factors were sent to DLP projector and projected onto the sample. Therefore several sets of raw images with the surface brightness levels of all pixels could be produced within the dynamic range of CCD camera. The raw images were reconstructed as high dynamic range images according to the calibration factors and were sent to phase-retrieving algorithm. Because of the images with larger signal-to-noise ratio from the high dynamic range, higher quality of 3-D data could be obtained.

To demonstrate the method, measured a slide mounted on a base plane with high reflectivity. Two grooves were formed with low reflectivity on the top of the slide by sand blasting. This study compared the measurement results between the traditional

fringe-projection moiré and the presented fringe-projection moiré system. The system included a DLP module, a uniform lighting module and a CCD camera. Firstly, aligned the system carefully and measured the relation between the pixel of the DLP and the pixel of CCD camera. Thereafter we could create a mapping table for looking up the intensity of the image which was captured by CCD camera according to the corresponding pixels on the DLP chip. The traditional fringe-projection moiré system and the DLP module provided uniform sine fringe over the whole field of the measurement. For solving the profile of the slide, the DLP module projected three sine-fringe images with a phase shift of $2\pi/3$ to the slide; and then the three-step phase-shifting algorithm was used to solve the profile, as shown in Fig. 6-3. The cross-sectional plot of the marked region of the slide is shown in the left-hand side of Fig. 6-3, and the horizontal axis stands for the pixels of CCD camera and the vertical axis is the height of the slide. The left-bottom image is one of the fringe image captured by CCD camera, indicating that the low reflectivity on the top of the slide made the image lose its contrast, owing to the contrast of the fringe was insufficient to perform the phase-retrieving algorithm. There were many spark noises in the darkest region.

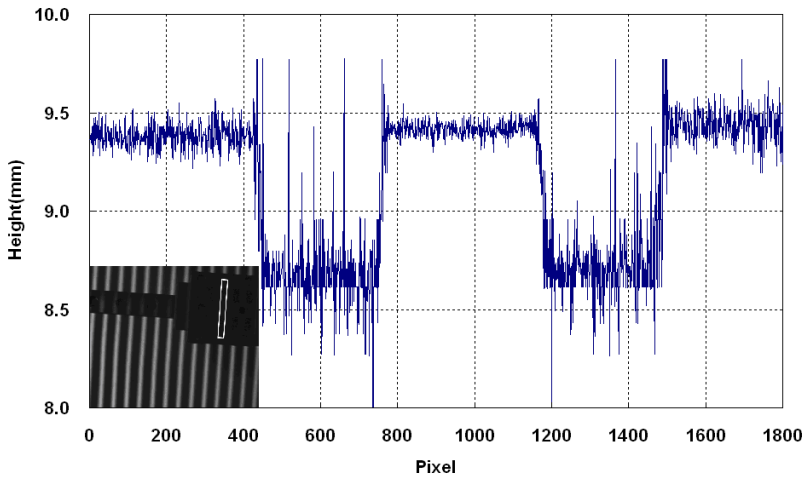

Fig. 6-3 The captured image and retrieved profile of the traditional fringe

projection

In order to overcome the insufficient contrast, the novel projection moiré system invoked the calibration module calculating the light intensity distribution over the field of view by modifying the edge detection algorithm and by defining the calibration factors for each region. Referring to the mapping table and using mixed-pixels algorithm, the measurement used the DLP module to adjust the average intensity and the average amplitude of the intensity modulation based on the factors and the fringes projected to the slide. The images captured by the CCD camera were then fed in the calibration module for the reconstruction of the high dynamic range images, as shown at the bottom-left of Fig. 6-4. After the process of the phase-retrieving algorithm, it obtained the 3D profile of the slide. Figure 6-4 shows the cross-sectional view of the marked region of the slide. Compared with Fig. 6-3, the contrast is adequate for performing the phase-retrieving algorithm leading to the high dynamic range image obtained from the intensity control unit. Hence the spark noise disappeared. This result demonstrated that the proposed method can successfully measure the objects with large dynamic surface reflectivity.

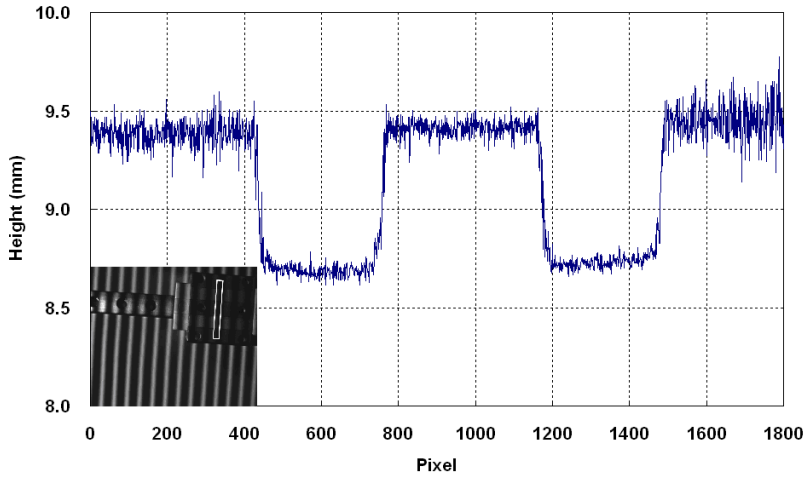

Fig. 6-4 The captured image and retrieved profile of the regional adjusting fringe projection

6.4 Conclusion

This chapter present 3D profile systems which are able to acquire a high dynamic range image in one-shot and preserve spatially resolution. An algorithm is proposed for calculating the calibration factors according to the different reflectivity for each region, and then the DLP module is designed for adjusting the illumination. A CCD camera is used for the capture of the image, and then an algorithm is performed for the reconstruction of the high dynamic range image by a compensation operation according to the calibration factors. This technique can improve the image contrast without reducing the spatial resolution and overcome the wide range of the variation of the surface reflectivity. Because a high dynamic range image is obtained by one-shot, it's economic without induced errors of multiple exposures. The enhanced fringe contrast by the high dynamic-range image provides the robustness of the phase-retrieving algorithms so that an accurate surface topography of a measured object can be obtained. The proposed method could be applicable to any optical measurement techniques that the reflectivity of the surface of the measured objects varies abruptly.

References

[1] Frank Chen, Gordon M. Brown, and Mumin Song, "Overview of three-dimensional shape measurement using optical methods," *Opt. Eng.*, vol. 39, 10-22, (2000).

[2] M. Sjodahl and P. Synnergren, "Measurement of shape by using projected random patterns and temporal digital speckle photography," *Appl. Opt.*, vol. 38, 1990-1997 (1999).

[3] E. Muller, "Fast three dimensional form measurement system," *Opt. Eng.*, vol. 34, 2754-2756 (1995).

[4] G. Sansoni, S. Corini, S. Lazzari, R. Rodella, and F. Docchio, "Three dimensional imaging based on gray-code light projection: characterization of the measuring algorithm and development of a measuring system for industrial application," *Appl. Opt.*, vol. 36, 4463-4472 (1997).

[5] Q. Hu, K. G. Harding, X. Du, and D. Hamilton, "Shiny parts measurement using color separation," *Proc. SPIE*, vol. 6000, 6000D1-8 (2005).

[6] R. Kokku and G. Brooksby, "Improving 3D surface measurement accuracy on metallic surfaces," *Proc. SPIE*, vol. 5856, 618-624 (2005).

[7] Song Zhang and Shing-Tung Yau, "High dynamic range scanning technique," *Opt. Eng.*, vol. 48, 033604 (2009).

[8] Shree K. Nayar and Tomoo Mitsunaga, "High dynamic range imaging: spatially varying pixel exposures," in *IEEE Conf. Computer Vision and Pattern Recognition*, vol. 1, 472-479 (2000).

[9] S. Zhang, X. Li, and S. T. Yau, "Multilevel quality-guided phase unwrapping algorithm for real-time three-dimensional shape reconstruction," *Appl. Opt.*, vol. 46, 50-57 (2007).

Chapter 7

Conclusions

Optical measurement techniques have been receiving an increasing attention during recent decades. The most important reason is that they work non-intrusively and therefore do not influence the investigated process. The continuing developments in laser, detector, optical fiber and computer technology will further augment the high applicability and versatility of optical measuring techniques. Therefore, it can be expected that optical techniques will continue to gain in importance in many fields of application. However, the procedures of optical measurement techniques include emitted a light signal, this signal modulated by device under test and analyzed the difference of those signal. The purpose of this dissertation is to discuss what is important in optical measurement technology is to adjust the light source suited with this measurement.

a. Thermo-Optic Tunable Tapered-Fiber Filter:

Broadband light sources with high spectral power density are important for high resolution optical coherence tomography (OCT) in cellular or tissue bio-imaging. The broadband light source with a smooth Gaussian power spectrum is advantageous to achieve low speckle noise, generating from the mutually coherent scattering photons from biological tissues. Echo free OCT imaging can be obtained since a non-Gaussian-spectrum light source will significantly distort the OCT axial point spread function. This dissertation has proposed a new method of achieving widely

tunable all-fiber broadband Gaussian-shaped spectral filters by concatenating thermo-optic tunable short-pass and long-pass filters. The material and waveguide dispersions are both employed to vary the spectral envelope of short-wavelength-pass filters and long-wavelength-pass filters to respectively fit the right and left wings of the desired Gaussian profile. The achieved spectral contrast can be higher than 40 dB and the filter still keeps Gaussian-shaped during thermo-tuning process. This kind of widely tunable Gaussian filters should be advantageous for optical coherence tomography (OCT) bio-imaging systems using broadband light sources.

This dissertation also presented a new type of thermo-optic tunable short-wavelength-pass fiber filters based on fiber tapering and dispersion engineering has been demonstrated experimentally and analyzed theoretically. Good agreements between the BPM simulation and experimental results are achieved. The effects of material dispersion and waveguide dispersion characteristics have been investigated by examining the spectral response as well as the changing trends of the MFD and the effective mode index. An optimized tapered fiber filter structure that can attain high-cutoff efficiency has been suggested based on the obtained theoretical simulation results. It finds for SMF-28 raw fibers, the uniform tapered waist diameter should be around 35μm, the uniform tapered-waist length should be greater than 30 mm, and the tapered-transition length should be greater than 6 mm. With such an optimized structure, the cutoff slope can be as high as -2.4dB/nm, the rejection efficiency can be as high as 70dB, and the fundamental mode-coupling loss is below 0.3dB. In principle, if different choices of raw fibers can be used, it is possible that the performance can be even more optimized. The analyses presented in the present work should be helpful for developing inline tapered fiber filters based on the dispersion-engineered fundamental-mode cutoff mechanism.

b. Supercontinuum Generation in a Tapered Fiber:

Supercontinuum generation from 1-μm tapered fiber using the 80 fs Ti:sapphire laser excitation is demonstrated experimentally and studied theoretically. By properly choosing the exciting wavelength, relatively wide spectra is observed from near UV to near IR only using 1-cm long and 1-μm-diameter optical tapered fiber. Besides, exciting power can be greatly lower down for wide spectra generation extended to near UV by properly connecting two fiber tapers. Split-step FFT method is investigated numerically in order to analyze the spectral response of supercontinuum generation phenomenon corresponding to the wavelength dependent loss occurred at transition region of the tapered fiber. The simulation results agree with the experimental results, and shows that the dispersion and nonlinear effects at transition region of the tapered fiber greatly influences the broaden spectrum shape. The theoretical result indicates that the zero dispersion cross point located at 2.6 μm so that the pulse width and peak power of the excited pulse is dramatically changed when propagates in transition region, which in term apparently affects the supercontinuum generation spectrum. Hopefully the simulation results in this work provide a helpful viewpoint to analyze the supercontinuum generation in typical tapered fibers.

c. Stable and Tunable Fiber Laser

This dissertation has proposed and investigates experimentally a tunable and stable fiber laser with single-longitudinal-mode output based on double-ring architecture. Double-ring structure provides a fine mode restriction and guarantees a single-longitudinal-mode operation. The output power of larger than −5 dBm and the side-mode suppression ratio of larger than 64.6 dB over the operating range from 1530 to 1560 nm can be obtained. And the maximum output power and side-mode

suppression ratio of the laser are 4.3 dBm and 70.2 dB at 1536 nm. In addition, the power fluctuation of less than 1 dB and the central wavelength variation of less than 0.04 nm also are observed for lasing wavelength in a short-term observing time.

d. Projection Moiré Profilometry with High-Dynamic Range Image:

This chapter present 3D profile systems which are able to acquire a high dynamic range image in one-shot and preserve spatially resolution. An algorithm is proposed for calculating the calibration factors according to the different reflectivity for each region, and then the DLP module is designed for adjusting the illumination. A CCD camera is used for the capture of the image, and then an algorithm is performed for the reconstruction of the high dynamic range image by a compensation operation according to the calibration factors. This technique can improve the image contrast without reducing the spatial resolution and overcome the wide range of the variation of the surface reflectivity. Because a high dynamic range image is obtained by one-shot, it’s economic without induced errors of multiple exposures. The enhanced fringe contrast by the high dynamic-range image provides the robustness of the phase-retrieving algorithms so that an accurate surface topography of a measured object can be obtained. The proposed method could be applicable to any optical measurement techniques that the reflectivity of the surface of the measured objects varies abruptly.

簡 歷

姓　名：周 森 益

性　別：男

籍　貫：台 北 市

學歷：

1990 ~ 1994　國立中山大學 物理系

1994 ~ 1996　國立中山大學 物理所　碩士班

論文題目：具光譜解析能力的共焦顯微鏡

2002 ~ 2012　國立交通大學 光電工程研究所　博士班

論文題目：應用於檢測技術的光源設計

經歷：

1998 ~ 2000　中山科學研究院 材料暨光電技術發展中心

2000 ~ 2004　康石科技股份有限公司

2006 ~ 迄今　工業技術研究院 量測技術發展中心